Ore Geology Reviews 66 (2015) 366–387

Contents lists available at ScienceDirect

Ore Geology Reviews

journal homepage: www.elsevier.com/locate/oregeorev

Trace metals in pyrite and marcasite from the Agua Rica porphyry-high sulfidation epithermal deposit, Catamarca, Argentina: Textural features and metal zoning at the porphyry to epithermal transition

Marta Franchini [a,b,*], Christopher McFarlane [c], Laura Maydagán [a,b,d], Martin Reich [e,f], David R. Lentz [c], Lawrence Meinert [g], Verónica Bouhier [a,b,d]

[a] CONICET, Argentina
[b] Departamento de Geología y Petróleo, Facultad de Ingeniería, Universidad Nacional del Comahue, Buenos Aires 1400, 8300 Neuquén, Argentina
[c] Department of Earth Sciences, University of New Brunswick, Fredericton, New Brunswick E3B 5A3, Canada
[d] Departamento de Geología, Universidad Nacional del Sur, San Juan 670, 8000 Bahía Blanca, Argentina
[e] Departamento de Geología, Universidad de Chile, Plaza Ercilla 803, Santiago, Chile
[f] Andean Geothermal Center of Excellence (CEGA), Universidad de Chile, Santiago, Chile
[g] U.S. Geological Survey, 12201 Sunrise Valley Drive, MS 913, Reston, VA 20192, United States

ARTICLE INFO

Article history:
Received 29 May 2014
Received in revised form 8 October 2014
Accepted 23 October 2014
Available online 1 November 2014

Keywords:
Trace elements
Pyrite–marcasite
Porphyry Cu
High sulfidation epithermal

ABSTRACT

Agua Rica is a world-class Cu (Mo–Au) deposit located in Catamarca, Argentina, in which the porphyry and high sulfidation epithermal stages are juxtaposed due to the telescoping of the mineralizing system. Pyrite is the most abundant sulfide in the analyzed section of the deposit and shows variations in textures and trace metal content (determined by LA–ICPMS), between the porphyry and epithermal stages. Pyrite from the porphyry stage is fine grained and depleted in most trace elements analyzed, except for traces of Co (up to 276 ppm) and Ni (up to 131 ppm). Pyrite from the epithermal stage is texturally complex, compositionally heterogeneous, and the trace metal content varies with depth and within sub-stages of mineralization. At an intermediate depth (2625 m), epithermal pyrite from the cement of the jig-saw and clast-supported hydrothermal breccias are enriched in Cu (up to 2961 ppm) that correlates with the highest Cu grades in the section. This pyrite contains micro-inclusions of sulfosalt minerals as inferred by LA–ICPMS elemental mapping and individual spot ablation profiles. They are zoned and show a Co-rich core, an intermediate zone enriched in Cu, and an outer rim rich in Zn. At shallower levels (3000 m), epithermal pyrite cements in the heterolithic hydrothermal breccia are unusually rich in trace metals that correlate with the highest Pb, Zn, Au, and Ag grades. The ore-stage pyrite occurs as either successive colloform bands on earlier Co-bearing cores or as veinlets infill. The colloform pyrite bands and veinlets are As-poor (<30 ppm) and enriched in Pb (up to 4528 ppm), Cu (up to 3900 ppm), Zn (up to 1078 ppm), Ag (up to 136 ppm), Au (up to 6.7 ppm), Bi (up to 1077 ppm), and Te (up to 3.1 ppm). In LA–ICPMS elemental maps, arsenic concentrates in a thin inner band within the thicker, trace element-rich rims. The colloform banding in pyrite is interpreted to reflect rapid crystallization during fluid boiling at a hydrothermal fluid–meteoric water interface, creating intense fluctuations in temperature and producing undercooling in the mixed fluid. This late and shallow fluid was depleted in As and Cu and also precipitated alunite, Fe-poor sphalerite, and marcasite enriched in trace metals. Maximum Au and Ag inputs into the system occurred towards the end of the epithermal cycle and are expressed by the Au–Ag-rich rims in hydrothermal pyrite. Based on Au–As data in pyrite, ore fluids forming early pyrite were undersaturated with respect to native Au (solid solution incorporation), while later fluids precipitating colloform pyrite were supersaturated with respect to native Au forming Au nanoparticles. This study provides evidence that pyrite records chemical changes at the porphyry to epithermal transition that can be used to monitor hydrothermal fluid evolution, constrain different mineralization stages, and vector towards undiscovered ore zones.

1. Introduction

Pyrite is widespread in hydrothermal ore deposits and previous studies have documented significant concentrations of Au, Ag, Cu, Pb, Zn, Co, Ni, As, Sb, Se, Te, Hg, Tl, and Bi, which in some cases can reach

---

* Corresponding author at: Consejo Nacional de Investigaciones Científicas y Técnicas.

http://dx.doi.org/10.1016/j.oregeorev.2014.10.022
0169-1368/

weight-percent levels (Cook and Chryssoulis, 1990; Cook et al., 2009; Deditius et al., 2011; Deditius et al., 2014; Large et al., 2009; Reich et al., 2005; Reich et al., 2006; Reich et al., 2013). Despite the fact that the trace-metal budget of pyrite has been heavily investigated in ore deposits where pyrite is a major Au-bearing ore mineral (i.e., Carlin-type and orogenic Au deposits), only a few studies have reported data in porphyry Cu deposits and epithermal Au systems (e.g., Chouinard et al., 2005; Deditius et al., 2009; Deditius et al., 2014; Maydagán et al., 2013; Reich et al., 2013; Zwahlen et al., 2014). Considering the fact that pyrite is ubiquitous in mineralized veins that represent the main locus of fluid flux in porphyry and epithermal systems, pyrite composition can complement mineralogical observations and fluid inclusion data, and provide further insights into metal budgets and changes in fluid composition (Deditius et al., 2014; Reich et al., 2013). Moreover, and considering recent evidence of Cu, Au, and As decoupling in pyrite from epithermal Au and porphyry Cu (e.g., Deditius et al., 2009; Reich et al., 2013, respectively), there is a need to better constrain the trace-element composition of pyrite throughout the porphyry to epithermal transition.

Here we document the compositional variation of pyrite and marcasite from the main section of the world-class Agua Rica Cu (Mo–Au) deposit in Catamarca, Argentina. This system presents a unique opportunity to constrain pyrite compositional systematics through the porphyry–epithermal transition, since sulfides and sulfosalts of Fe, Cu, Mo, As, Zn, Pb, Sn, and Bi, and related invisible Au–Ag mineralization precipitated during the porphyry through to high-sulfidation epithermal stages; they are juxtaposed due to telescoping of this system, so that they are now exposed at the same level of erosion (Franchini et al., 2011, 2012).

Pyrite is the most abundant sulfide in the deposit and shows differen textures, including replacement and dissolution–reprecipitation processes evident from scanning electron microscopy (SEM) backscatter electron (BSE) imaging, and compositions that are easily recognized even when the porphyry and high-sulfidation epithermal stages of mineralization are superposed within the same sample. For example, in the phyllic envelope, pyrite is fine grained and anhedral. Coarser grained pyrite typical of the epithermal stage shows colloform overgrowths and at least three generations of pyrite have been identified in hydrothermal breccias. Marcasite occurs in minor amounts in hydrothermal breccias filling interstices between pyrite and other sulfides. Previous studies reporting electron microprobe analyzer (EMPA) data have documented trace element-enriched rims relative to the cores in some of these pyrite crystals (Franchini et al., 2011), suggesting the presence of multiple fluid pulses and differential partitioning of metals into pyrite at Agua Rica.

In this study, the trace-element composition of well-constrained pyrite and marcasite samples from Agua Rica was obtained using laser ablation–inductively coupled plasma mass spectrometer (LA–ICPMS) techniques. We show that the trace-element database of pyrite from Agua Rica can help: a) to constrain variations in the pyrite composition over the transition from porphyry to the epithermal stages, and thus evaluate the use of trace elements in pyrite as vectors in exploration, b) to define the paragenetic relations among the various bands of colloform pyrite, marcasite, and the polymetallic zinc (sphalerite), lead (aikinite), bismuth (emplectite), gold, and silver (invisible) mineralization that are still not well defined, and c) analyze to what extent these changes in fluid composition and precipitation mechanisms in the high sulfidation epithermal environment influence pyrite composition overall. Furthermore, and in the light of recent studies documenting the geochemical behavior of Au, As, and Cu in hydrothermal systems (Deditius et al., 2009; Deditius et al., 2014; Reich et al., 2013), we explore the role of pyrite as a scavenger of metals and its use as a marker of changing physiochemical conditions of saturation throughout the transition from the porphyry mineralized system to the epithermal mineralization.

2. Geology of the deposit

Agua Rica is located at the northern end of the Sierras Pampeanas geological province close to the southern margin of the Puna geological province and separated by the NE-striking Tucumán Transfer Zone (Urreiztieta et al., 1993). The region contains Precambrian to early Paleozoic folded metamorphic rocks (Koukharsky and Mirré, 1976) and Paleozoic granitic rocks (422.7 ± 6.1 and 438.4 ± 6.3 Ma, K–Ar muscovite ages, Capillitas–Belén granite suite; Caelles et al., 1971; Koukharsky and Mirré, 1976). These rocks have been intruded by the Farallón Negro Volcanic Complex (FNVC, 12.56–5.16 Ma; Sasso, 1997; Sasso and Clark, 1998) — the easternmost manifestation of Neogene volcanic activity in this area with a basin and range topography (Jordan and Allmendinger, 1986; Fig. 1A). The FNVC in the study area is represented by the Melcho porphyry (8.56 ± 0.48 Ma, Ar–Ar age in hornblende; Sasso, 1997; Sasso and Clark, 1998), the Trampeadero and the Seca Norte alkaline and high K, feldspar porphyries (5.10 ± 0.05 Ma, K–Ar age of hydrothermal biotite; Perelló et al., 1998) with multiple intrusive facies (Landtwing et al., 2002; Perelló et al., 1998), and various breccia types, the volumetrically most prominent being a hydrothermal breccia that is exposed south and southeast of the Agua Rica camp, along the Quebrada Minas lineament (Fig. 1A). Several small porphyritic bodies have been mapped along the margin of the deposit (distal porphyries; Landtwing et al., 2002; Fig. 1A). The porphyries and breccias were emplaced along the SE-striking Quebrada Minas lineament. East–west striking, south-dipping normal faults were active both syn- and post-mineralization. The Agua Rica camp structure has the same orientation as the Quebrada Seca Fault and may have controlled emplacement of the biotite porphyry. West-southwest dipping low-angle reverse faults (Fig. 1A) have structurally thickened the leached capping on the west side of the deposit, and the thrusted granite–metasedimentary rock contact has the same geometry (Landtwing et al., 2002).

3. Alteration and mineralization

Agua Rica is a world class Cu (Mo–Au) deposit in which the porphyry and high sulfidation epithermal stages, usually ~1 km vertically separated, are exposed at the same erosional level. Telescoping is interpreted as a consequence of the progressive degradation of the paleosurface (exhumation) due to regional uplift of Sierras Pampeanas along NE-striking faults (Allmendinger, 1986; Jordan and Allmendinger, 1986; Sasso, 1997; Sasso and Clark, 1998; Bissig et al., 2001). Previous investigations (BHP, 1999; Koukharsky and Mirré, 1976; Landtwing et al., 2002; Navarro, 1986; Perelló et al., 1998; Rojas et al., 1998; Rosco and Koukharsky, 1999; Sasso, 1997) document a complex history of overprinting stages of subvolcanic intrusions, mineralization, brecciation, and erosion at Agua Rica. Franchini et al. (2011, 2012) presented a detailed description of the distribution of the hydrothermal alteration and mineralization along the east–west 6969400 main section, where the Seca Norte (west) and the Trampeadero porphyries have intruded the metasedimentary rocks and are in turn cut by igneous and hydrothermal breccias and sandy (pyroclastic) dikes (Fig. 1B). In this section, relic early, high temperature (370 °C to >550 °C) potassic alteration (Fig. 1C) with high Cu (0.11–0.6% Cu) and low Mo (average = 196 ppm) grades is encapsulated in a phyllic halo (Fig. 1C) with a mineral assemblage that suggests temperatures of formation of ≤350 °C and high sulfur fugacity. This stage was Mo-rich (>1000 ppm), did not add Cu, Au, and As in the altered zone, and some of the stockwork quartz veinlets have been striped/leached of their former sulfides.

An early stage of advanced argillic alteration was barren and precipitated andalusite (~360 °C–375 °C) clots in the roots (Fig. 1C), pyrophyllite (280 °C–360 °C) at intermediate levels, and vuggy silica (<250 °C) in the uppermost levels of the alteration halo. A new emplacement of magma at shallow depth and resulting fluid exsolution, expansion, and unroofing, produced hydrothermal brecciation (interfingering granite and hydrothermal breccias) and subsequent multistage

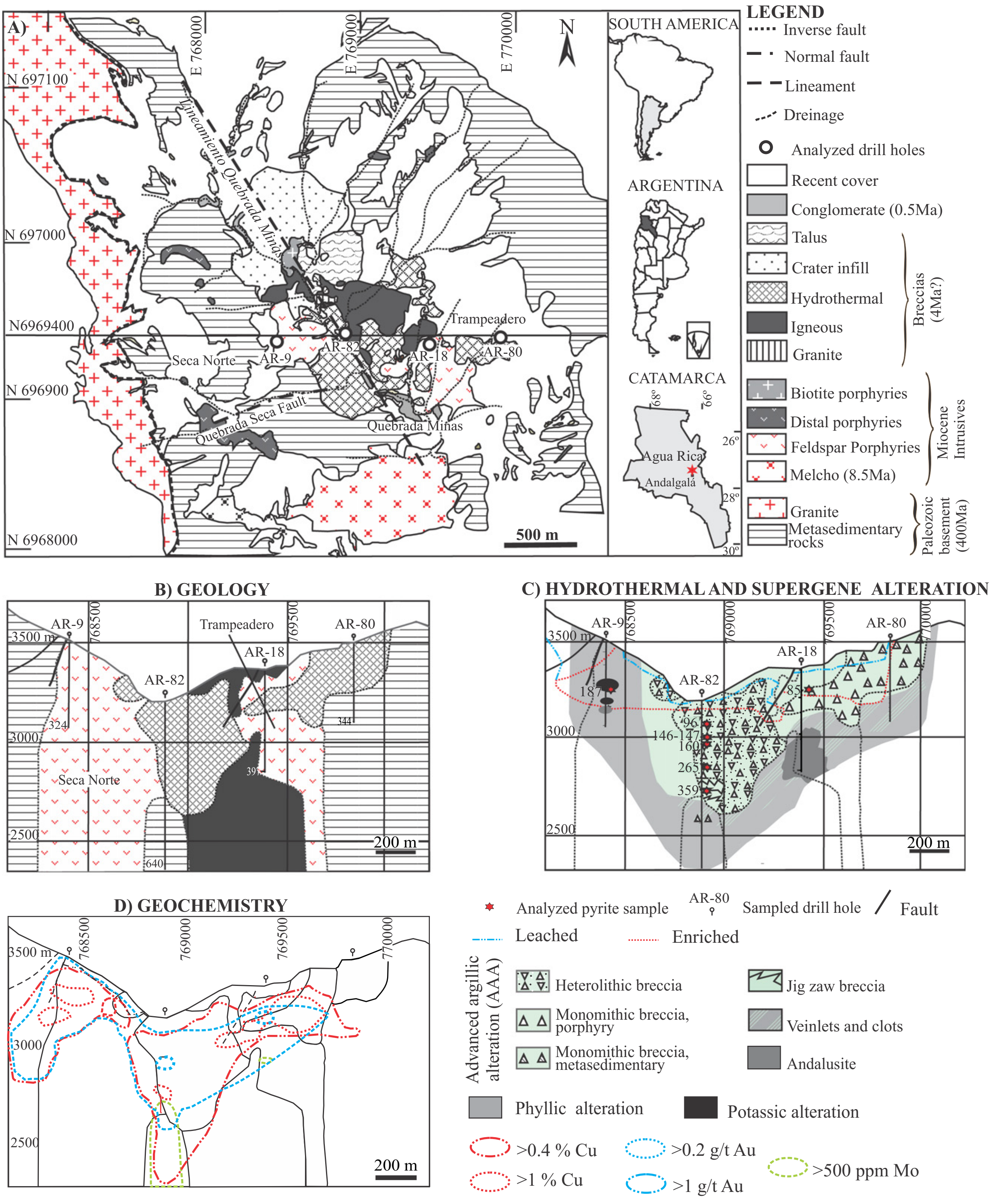

Fig. 1. A) Geological map of the Agua Rica district with the location of the E-O 6969400 N cross-section and sampled drill holes (modified from BHP, 1999; Landtwing et al., 2002). B) Geology of the E-O section along 6969400 N with the location of sampled drill holes and analyzed pyrite samples (modified from BHP, 1999). C) Lateral and vertical distribution of hydrothermal and supergene alteration types along the section. D) Geochemistry (modified from BHP, 1999; Franchini et al., 2011).

advanced argillic alteration and mineralization (Fig. 1C). These fluids precipitated an intermediate temperature advanced argillic paragenesis with Fe–Cu–As–Sn sulfides and sulfosalts as cement in the deepest parts of the hydrothermal breccias located in the center of the section (Figs. 1C, 2; jigsaw breccia). This zone contains the highest grades of hypogene Cu and As (up to 3.7% Cu and 0.27% As), with traces of Zn (up to 0.3%) and Pb (0.13%) (Figs. 1D, 2). At higher elevations (10 to 196 m depth), the breccia becomes matrix-supported with local evidence of

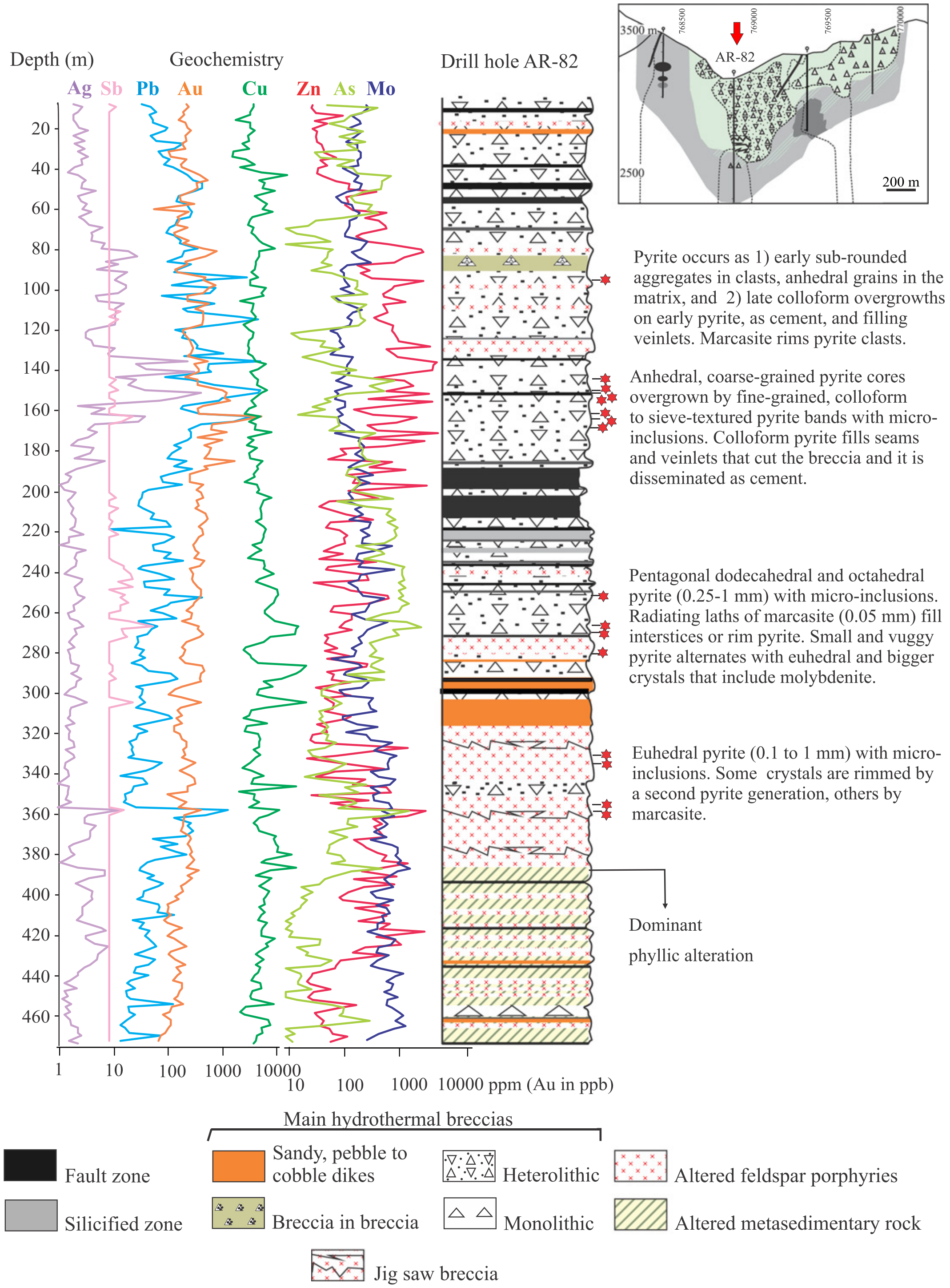

Pyrite occurs as 1) early sub-rounded aggregates in clasts, anhedral grains in the matrix, and 2) late colloform overgrowths on early pyrite, as cement, and filling veinlets. Marcasite rims pyrite clasts.

Anhedral, coarse-grained pyrite cores overgrown by fine-grained, colloform to sieve-textured pyrite bands with micro-inclusions. Colloform pyrite fills seams and veinlets that cut the breccia and it is disseminated as cement.

Pentagonal dodecahedral and octahedral pyrite (0.25-1 mm) with micro-inclusions. Radiating laths of marcasite (0.05 mm) fill interstices or rim pyrite. Small and vuggy pyrite alternates with euhedral and bigger crystals that include molybdenite.

Euhedral pyrite (0.1 to 1 mm) with micro-inclusions. Some crystals are rimmed by a second pyrite generation, others by marcasite.

Dominant phyllic alteration

Fig. 2. Geochemistry, geology, alterations and pyrite textures of the advanced argillic alteration cut by drill hole AR-82 in the N 6969400 section. Data are based on BHP (1999) and Franchini et al. (2011).

more than one episode of brecciation (Figs. 1C, 2). Copper and As grades in this breccia zone are lower (0.2–0.6% Cu, 0.001–0.03% As), but Zn (0.1–0.55%) and Pb (0.1–0.53%; Figs. 1D, 2) grades are higher. High Au and Ag grades (1–5.6 g/t Au and 239–325 g/t Ag) display a positive correlation with Pb and Zn. Hypogene Cu grades notably decrease eastwards (>1% Cu), with sectors up to 3.4% Cu in the brecciated Trampeadero porphyry towards <0.35% Cu in the brecciated metasedimentary rock (Fig. 1D), as does Zn, Au, and Pb, whereas As contents are higher in the brecciated metasedimentary rock. Dickite and kaolinite occur in the advanced argillic and phyllic halos as late minerals in clots or in veinlets thus, in these zones, fluid cooled enough for their formation. For more details refer to Franchini et al. (2011, 2012).

4. Analytical methods

Seventy-two samples of hydrothermally altered rocks were collected from 4 BHP drill cores of the main section. Fig. 1A, B, and C shows drill-hole locations in the east–west cross-section 6969400 N across the Agua Rica deposit. Textures and sulfide–gangue relationships were examined first in drill cores samples using a binocular microscope and

Table 1A
Selected trace element analyses of pyrite and marcasite determined by LA–ICPMS.

Average minimum detection limit (MDL) ppm			0.002	Int2SE	0.171	0.003	0.005	0.500	0.009	0.002	0.034	0.004	0.055	0.040	0.710	0.650	0.100	0.037	0.015	0.019	0.200
Porphyry stage																					
Sample no.	**Analysis**	**Comments**	**Au (ppm)**	**Au ppm**	**As (ppm)**	**Ag (ppm)**	**Co (ppm)**	**Ni (ppm)**	**Pb (ppm)**	**Bi (ppm)**	**Te (ppm)**	**Mo (ppm)**	**V (ppm)**	**Cu (ppm)**	**Zn (ppm)**	**Mn (ppm)**	**Ge (ppm)**	**Cd (ppm)**	**Sn (ppm)**	**Sb (ppm)**	**Hg (ppm)**
AR18-85 m	Py. 1.1	Fractured crystal in vein	0.009	0.004	2.720	0.028	276.000	5.200	0.393	0.527	<0.034	<0.004	0.038	87.000	<0.71	<0.65	1.340	0.035	0.013	<0.019	N.A.
AR18-85 m	Py. 1.2	Fractured crystal in vein	<0.002	0.000	1.740	0.001	33.900	17.600	0.008	0.001	<0.034	<0.004	0.042	2.100	<0.71	<0.65	1.260	<0.037	0.007	<0.019	N.A.
AR18-85 m	Py. 1.3	Fractured crystal in vein	0.011	0.005	2.460	0.018	166.800	17.800	0.540	0.243	<0.034	0.006	0.060	38.000	0.510	<0.65	1.280	0.008	0.020	0.019	N.A.
AR18-85 m	Py. 1.4	Fractured crystal in vein	0.001	0.001	2.460	0.003	189.000	4.500	0.016	0.016	0.021	0.003	<0.055	5.300	0.270	<0.65	1.180	0.009	0.022	<0.019	N.A.
AR18-85 m	Py. 1.5	Fractured crystal in vein	<0.002	0.001	1.880	0.002	159.700	1.890	0.004	0.006	<0.034	<0.004	0.017	2.200	<0.71	<0.65	1.190	0.007	0.012	<0.019	N.A.
Average			*0.007*	*0.002*	*2.252*	*0.010*	*165.080*	*9.398*	*0.192*	*0.158*	*0.021*	*0.005*	*0.039*	*26.920*	*0.390*		*1.250*	*0.015*	*0.015*	*0.019*	
AR9-187 m	Py. 1.1	Anhedral crystal, core	<0.002	0.001	0.080	0.001	26.400	3.230	0.017	0.002	<0.034	0.002	0.024	0.850	0.110	<0.65	1.150	<0.037	0.020	0.005	N.A.
AR9-187 m	Py. 1.2	Anhedral crystal, mid-section	<0.002	0.000	<0.17	<0.003	30.500	4.380	<0.009	<0.002	<0.034	<0.004	0.039	0.790	<0.71	<0.65	1.180	0.018	0.011	<0.019	N.A.
AR9-187 m	Py. 1.3	Anhedral crystal, mid-section	0.002	0.002	<0.17	<0.003	56.800	8.700	0.024	0.002	<0.034	0.002	0.042	2.400	0.720	<0.65	1.080	<0.037	0.012	<0.019	N.A.
AR9-187 m	Py. 2.1	Anhedral crystal, rim	<0.002	0.001	0.840	0.004	58.200	131.000	0.060	0.074	0.198	<0.004	0.058	14.000	<0.71	<0.65	1.190	<0.037	0.007	0.008	N.A.
AR9-187 m	Py. 2.2	Anhedral crystal, core	0.001	0.001	0.170	0.002	110.000	3.260	<0.009	0.001	<0.034	<0.004	0.018	1.500	<0.71	0.590	1.180	0.026	0.009	<0.019	N.A.
AR9-187 m	Py. 2.3	Anhedral crystal, rim	<0.002	0.000	0.180	0.001	127.000	12.800	0.023	0.001	<0.034	0.003	0.011	1.050	0.180	0.410	1.200	0.016	<0.015	0.004	N.A.
Average			*0.001*	*0.001*	*0.318*	*0.002*	*68.150*	*27.228*	*0.031*	*0.016*	*0.198*	*0.002*	*0.032*	*3.432*	*0.337*	*0.500*	*1.163*	*0.020*	*0.012*	*0.006*	

Abbreviations: Cv: covellite, Int2SE: analytical error, N.A.: not analyzed, Mcr: marcasite, Py: pyrite. Notes: The internal standard used was Fe for pyrite and marcasite (460000 ppm).

Table 1B
Selected trace element analyses of pyrite and marcasite determined by LA–ICPMS.

Average minimum detection limit (MDL) ppm			0.002	Int2SE	0.171	0.003	0.005	0.500	0.009	0.002	0.034	0.004	0.055	0.040	0.710	0.650	0.100	0.037	0.015	0.019	0.200
Epithermal stage. Heterolithic, matrix-supported hydrothermal breccia																					
Sample no.	**Analysis**	**Comments**	**Au (ppm)**	**Au ppm**	**As (ppm)**	**Ag (ppm)**	**Co (ppm)**	**Ni (ppm)**	**Pb (ppm)**	**Bi (ppm)**	**Te (ppm)**	**Mo (ppm)**	**V (ppm)**	**Cu (ppm)**	**Zn (ppm)**	**Mn (ppm)**	**Ge (ppm)**	**Cd (ppm)**	**Sn (ppm)**	**Sb (ppm)**	**Hg (ppm)**
AR82-96 m	Py. 1.1	Clast, core	<0.002	0.003	<0.17	<0.003	7.600	1.600	0.122	0.145	0.190	0.006	N.A.	2.200	1.400	<1.1	2.260	0.029	<0.014	0.080	0.050
AR82-96 m	Py. 1.2	Clast, core	0.002	0.004	<0.17	0.006	21.700	2.720	0.130	0.027	<0.00734	0.000	N.A.	2.300	0.660	<1.7	2.040	<0.004	0.006	<0.075	<0.033
AR82-96 m	Py. 1.3	Clast, mid-section	<0.002	0.003	0.610	0.006	1.590	0.240	0.020	0.031	<0.1091	0.000	N.A.	3.300	0.790	<0.1	1.800	<0.03	0.010	<0.012	0.250
AR82-96 m	Py .1.4	Clast, rim	0.004	0.005	<0.17	0.041	19.100	4.090	1.940	1.800	0.250	0.000	N.A.	9.200	0.200	<1.1	2.110	0.023	0.009	<0.005	0.240
AR82-96 m	Py. 1.5	Clast, rim	0.249	0.067	0.550	3.260	0.183	0.390	6.900	0.660	0.190	0.000	N.A.	11.000	5.800	<0.6	2.030	0.034	0.030	0.036	0.040
Average			*0.085*	*0.016*	*0.580*	*0.828*	*10.035*	*1.808*	*1.822*	*0.533*	*0.210*	*0.001*		*5.600*	*1.770*		*2.048*	*0.029*	*0.014*	*0.058*	*0.145*
AR82-96 m	Py. 2.1	Elongated clast	<0.002	0.004	<0.17	0.023	121.600	26.500	0.090	0.029	0.000	0.000	N.A.	4.100	0.900	<1.6	2.000	<0.043	0.051	<0.068	0.260
AR82-96 m	Py. 2.2	Elongated clast	<0.002	0.004	<0.17	0.017	41.600	5.530	0.084	0.274	0.035	0.000	N.A.	3.900	0.600	<0.3	2.090	0.079	0.006	0.043	0.150
AR82-96 m	Py. 2.3	Anhedral clast	0.011	0.007	4.030	0.038	194.100	15.400	7.000	3.590	0.630	0.129	N.A.	4.400	7.500	6.200	1.680	<0.001	1.520	<0.067	0.070
Average			*0.011*	*0.005*	*4.030*	*0.026*	*119.100*	*15.810*	*2.391*	*1.298*	*0.222*	*0.043*		*4.133*	*3.000*	*6.200*	*1.923*	*0.079*	*0.526*	*0.043*	*0.160*
AR82-96 m	Py. 2.1	Veinlet in clast	0.155	0.005	1.850	0.611	18.290	9.700	2.230	0.944	<0.034	0.071	0.410	574.000	2.400	0.990	1.220	0.051	3.900	0.175	N.A.
AR82-96 m	Py. 2.2	Veinlet in clast	0.328	0.038	1.610	1.510	17.800	14.000	1.930	1.000	0.046	0.032	0.049	49.000	0.710	1.200	1.830	0.032	0.210	0.061	N.A.
AR82-96 m	Py. 2.3	Veinlet in clast	<0.002	0.014	<0.17	0.005	1.250	1.230	0.054	0.021	0.038	<0.004	<0.055	373.000	0.230	0.780	1.600	0.056	0.027	0.012	N.A.
AR82-96 m	Py. 2.4	Veinlet in clast	<0.002	0.011	0.220	0.002	31.480	21.700	0.129	0.022	<0.034	<0.004	0.059	21.500	<0.71	1.100	1.740	0.068	0.028	0.008	N.A.
Average			*0.242*	*0.017*	*1.227*	*0.532*	*17.205*	*11.658*	*1.086*	*0.497*	*0.042*	*0.052*	*0.173*	*254.375*	*1.113*	*1.018*	*1.598*	*0.052*	*1.041*	*0.064*	
AR82-96 m	Py. 3.1	Anhedral in clast	0.007	0.005	<0.17	0.033	3.370	6.480	0.860	0.255	0.000	0.000	N.A.	56.000	1.130	0.100	1.800	0.009	0.007	0.033	0.010
AR82-96 m	Py. 3.2	Anhedral in clast	0.352	0.070	<0.17	2.600	23.300	37.300	1.860	154.000	0.800	0.000	N.A.	1090.000	1.200	1.300	2.180	0.014	0.085	0.023	<0.11
AR82-96 m	Py. 3.3	Anhedral in clast	0.016	0.011	0.090	0.023	25.900	44.000	0.440	0.503	1.160	0.000	N.A.	66.600	0.300	0.600	1.540	<0.022	0.080	0.006	0.110
Average			*0.125*	*0.029*	*0.090*	*0.885*	*17.523*	*29.260*	*1.053*	*51.586*	*0.653*	*0.000*		*404.200*	*0.877*	*0.667*	*1.840*	*0.012*	*0.057*	*0.021*	*0.060*
AR82-96 m	Py. 4.3	Veinlet in clast	0.055	0.019	4.500	0.406	121.400	72.300	4.570	0.692	<0.081	0.047	N.A.	15.400	24.000	1.200	2.300	0.100	0.067	<0.066	0.090
AR82-96 m	Py. 4.4	Veinlet in clast	0.132	0.032	40.700	0.036	28.300	40.700	21.900	0.960	0.150	0.151	N.A.	56.000	8.500	9.100	1.820	0.046	1.620	0.096	<0.23
Average			*0.094*	*0.026*	*22.600*	*0.221*	*74.850*	*56.500*	*13.235*	*0.826*	*0.150*	*0.099*		*35.700*	*16.250*	*5.150*	*2.060*	*0.073*	*0.844*	*0.096*	*0.090*
AR82-96 m	Mcr. 5.1	Very fine-grained cement	0.550	0.110	28.700	66.000	0.035	0.160	33.000	162.000	0.560	0.000	N.A.	8940.000	8.000	2.500	2.070	0.003	0.980	2.210	0.450
AR82-96 m	Mcr. 5.2	Very fine-grained cement	6.590	0.410	81.800	940.000	0.236	1.590	1437.000	241.000	5.600	0.008	N.A.	2830.000	5710.000	4.700	1.830	0.450	22.700	4.220	0.170
AR82-96 m	Mcr. 5.3	Very fine-grained cement	6.120	0.530	90.200	668.000	0.790	0.870	1130.000	203.300	3.800	0.000	N.A.	3500.000	59000.000	2.000	2.250	27.300	19.260	5.210	0.490
AR82-96 m	Mcr. 5.4	Very fine-grained cement	1.600	0.170	11.700	21.300	128.600	43.100	106.700	57.900	1.070	0.300	N.A.	6390.000	11.900	1.500	1.930	0.190	0.465	0.980	0.250
Average			*3.715*	*0.305*	*53.100*	*423.825*	*32.415*	*11.430*	*676.675*	*166.050*	*2.758*	*0.077*		*5415.000*	*16182.475*	*2.675*	*2.020*	*6.986*	*10.851*	*3.155*	*0.340*
A82-146 m A	Py. 1.1	Clast, core	0.003	0.002	0.180	0.018	46.000	16.520	0.021	0.041	0.000	0.000	N.A.	4.370	0.360	<0.11	1.760	0.021	0.012	0.002	0.076
A82-146 m A	Py. 1.2	Clast, core	0.031	0.015	0.470	0.880	119.100	17.770	50.000	0.900	0.000	1.610	N.A.	185.000	4.400	1.470	1.920	0.017	0.025	0.044	0.001
A82-146 m A	Py. 2.2	Clast, core	0.001	0.001	0.110	0.114	138.000	14.100	0.430	0.131	0.049	0.008	N.A.	7.700	0.740	0.480	1.910	0.020	0.610	<0.01	0.022
Average			*0.012*	*0.006*	*0.253*	*0.337*	*101.033*	*16.130*	*16.817*	*0.357*	*0.016*	*0.539*		*65.690*	*1.833*	*0.975*	*1.863*	*0.019*	*0.216*	*0.023*	*0.033*
A82-146 m A	Py. 2.1	Anhedral, colloform rim	4.890	0.150	5.530	108.700	1.990	6.370	376.000	129.400	1.140	19.600	N.A.	3660.000	57.600	3.690	1.910	0.186	0.552	0.568	0.185
A82-146 m A	Py. 2.3	Anhedral, colloform rim	4.830	0.160	12.530	104.400	18.400	4.390	2410.000	156.600	2.280	1.400	N.A.	3650.000	520.000	38.900	1.710	0.442	0.743	0.517	0.187
A82-146 m A	Py. 3.1	Anhedral, colloform, fine-grained	5.480	0.210	17.290	121.800	1.930	0.920	3330.000	169.200	2.200	0.880	N.A.	3149.000	563.000	49.200	1.630	0.550	0.734	0.691	0.312
A82-146 m A	Py. 3.2	Anhedral,colloform, fine-grained	3.384	0.090	4.630	119.800	1.209	2.750	279.900	97.500	1.050	12.110	N.A.	3900.000	26.700	1.980	1.720	0.214	0.542	0.683	0.027
Average			*4.646*	*0.153*	*9.995*	*113.675*	*5.882*	*3.608*	*1598.975*	*138.175*	*1.668*	*8.498*		*3589.750*	*291.825*	*23.443*	*1.743*	*0.348*	*0.643*	*0.615*	*0.178*
A82-146 m B	Py. 5.1	Veinlet, core	0.045	0.011	0.800	1.956	6.900	3.470	268.400	2.120	0.014	0.000	N.A.	888.000	31.200	2.320	1.820	0.152	0.058	<0.013	<0.003
A82-146 m B	Py. 5.2	Veinlet, core	1.461	0.073	8.980	23.280	19.600	6.580	1680.000	29.300	0.470	0.000	N.A.	1177.000	142.900	26.500	2.120	0.600	0.244	0.149	0.012
Average			*0.753*	*0.042*	*4.890*	*12.618*	*13.250*	*5.025*	*974.200*	*15.710*	*0.242*	*0.000*		*1032.500*	*87.050*	*14.410*	*1.970*	*0.376*	*0.151*	*0.149*	*0.012*
A82-146 m B	Py. 5.3	Stringer, core	3.660	0.220	21.440	80.800	3.200	1.450	4300.000	123.900	2.720	0.020	N.A.	2270.000	1078.000	84.600	2.330	1.810	0.498	0.461	0.134
A82-146 m B	Py. 6.1	Stringer, colloform rim	3.010	0.140	22.150	55.200	22.400	11.120	4528.000	80.400	1.320	0.250	N.A.	1316.000	893.000	87.000	2.960	4.510	0.366	0.511	0.041
A82-146 m B	Py. 6.2	Stringer, colloform rim	3.510	0.150	24.500	57.300	11.840	3.920	4150.000	79.300	1.650	0.009	N.A.	1445.000	796.000	84.100	3.660	5.180	0.309	0.636	0.162
A82-146 m B	Py. 6.3	Stringer, colloform rim	4.000	0.140	25.190	73.400	11.400	3.030	4480.000	100.800	1.960	0.270	N.A.	2210.000	908.000	96.700	3.370	5.020	0.346	0.582	0.172
Average			*3.545*	*0.163*	*23.320*	*66.675*	*12.210*	*4.880*	*4364.500*	*96.100*	*1.913*	*0.137*		*1810.250*	*918.750*	*88.100*	*3.080*	*4.130*	*0.380*	*0.548*	*0.127*
A82-146 m C	Py. 7.1	Clast, first generation	0.001	0.001	<0.1	0.005	11.870	43.400	0.035	0.022	0.000	0.000	N.A.	4.400	0.730	0.170	1.590	0.000	0.027	0.005	<0.019
A82-146 m C	Py. 7.2	First generation	0.002	0.002	0.150	0.013	14.320	40.500	0.138	0.012	0.000	0.000	N.A.	5.400	0.040	0.350	1.710	<0.023	0.010	0.000	0.035

(continued on next page)

Table 1B *(continued)*

Average minimum detection limit (MDL) ppm			0.002	Int2SE	0.171	0.003	0.005	0.500	0.009	0.002	0.034	0.004	0.055	0.040	0.710	0.650	0.100	0.037	0.015	0.019	0.200
A82-146 m C	Py. 8.1	First generation	0.005	0.003	0.080	0.101	10.990	11.500	4.700	0.124	0.000	0.000	N.A.	55.000	4.390	<0.08	1.450	<0.003	0.018	0.025	0.010
A82-146 m C	Py. 10.1	First generation	0.111	0.035	0.490	2.410	28.400	8.600	340.000	1.960	<0.012	0.018	N.A.	450.000	54.000	4.000	1.590	0.151	0.049	0.037	0.080
Average			*0.030*	*0.010*	*0.240*	*0.632*	*16.395*	*26.000*	*86.218*	*0.529*	*0.000*	*0.005*		*128.700*	*14.790*	*1.507*	*1.585*	*0.076*	*0.026*	*0.017*	*0.042*
A82-146 m C	Py. 7.3	Second generation, colloform	1.241	0.086	4.540	15.400	33.100	41.500	746.000	18.600	0.230	0.000	N.A.	577.000	67.000	11.200	1.520	0.124	0.072	0.086	<0.012
A82-146 m C	Py. 8.2	Second generation, colloform	6.730	0.380	19.800	121.900	2.010	0.390	4190.000	184.000	1.200	0.009	N.A.	1820.000	764.000	76.600	1.720	0.810	2.000	0.626	0.160
A82-146 m C	Py. 8.3	Second generation, colloform	5.800	0.440	18.500	86.500	6.100	1.970	4040.000	120.600	1.170	3.640	N.A.	2230.000	573.000	57.400	1.430	0.536	0.249	0.484	0.200
A82-146 m C	Py. 10.2	Second generation, colloform	4.720	0.170	10.540	107.700	0.960	2.240	3030.000	145.700	1.710	0.670	N.A.	2700.000	1045.000	66.700	1.580	0.850	0.489	0.422	0.290
A82-146 m C	Py. 10.3	Second generation, colloform	3.140	0.270	6.700	37.900	132.000	31.400	1050.000	36.700	0.270	44.000	N.A.	873.000	107.000	23.300	1.520	0.560	0.136	0.109	0.234
Average			*4.326*	*0.269*	*12.016*	*73.880*	*34.834*	*15.500*	*2611.200*	*101.120*	*0.916*	*9.664*		*1640.000*	*511.200*	*47.040*	*1.554*	*0.576*	*0.589*	*0.345*	*0.221*
A82-146 m C	Py. 9.1	Third generation, colloform	4.900	0.440	14.300	64.500	30.900	17.360	2650.000	93.000	1.050	4.270	N.A.	1610.000	383.000	44.500	1.500	0.570	1.710	0.287	0.230
A82-146 m C	Py. 9.2	Third generation, colloform	2.120	0.110	6.430	37.600	12.800	7.920	1106.000	51.000	0.270	0.000	N.A.	583.000	100.000	17.800	1.400	0.205	0.078	0.142	0.071
A82-146 m C	Py. 9.3	Third generation, colloform	2.850	0.130	8.040	40.300	10.590	3.510	1482.000	54.600	0.500	2.040	N.A.	1096.000	204.600	26.300	1.630	0.284	0.193	0.207	0.175
Average			*3.290*	*0.227*	*9.590*	*47.467*	*18.097*	*9.597*	*1746.000*	*66.200*	*0.607*	*2.103*		*1096.333*	*229.200*	*29.533*	*1.510*	*0.353*	*0.660*	*0.212*	
A82-146 m D	Py. 4.1	Subhedral in clast	0.001	0.001	0.210	0.000	829.000	8.970	0.003	<0.0023	<0.01485	0.000	N.A.	0.780	0.380	0.290	1.620	<0.016	0.014	0.036	<0.059
A82-146 m D	Py. 4.2	Subhedral in clast	0.000	0.000	0.120	0.007	322.000	43.500	0.013	0.001	0.000	0.000	N.A.	1.950	0.200	0.110	1.660	<0.032	0.005	<0.006	0.067
A82-146 m D	Py. 4.3	Subhedral in clast, rim	0.150	0.045	4.990	3.530	140.900	34.500	420.000	3.330	0.092	0.003	N.A.	373.000	31.200	9.400	1.810	0.375	0.035	0.048	0.106
Average			*0.050*	*0.015*	*1.773*	*1.179*	*430.633*	*28.990*	*140.005*	*1.666*	*0.046*	*0.001*		*125.243*	*10.593*	*3.267*	*1.697*	*0.375*	*0.018*	*0.042*	
A82-147 m	Py. 1.1	Clast rim	0.026	0.002	0.180	0.330	114.000	161.000	0.820	4.900	<0.032	0.003	0.021	35.200	<0.29	0.000	1.980	0.021	0.007	0.042	N.A.
A82-147 m	Py. 1.2	Clast rim	0.110	0.130	15.080	0.011	119.600	97.000	0.003	0.630	0.013	0.005	<0.034	2.500	0.110	1.000	1.640	0.053	<0.003	0.017	N.A.
A82-147 m	Py. 1.3	Clast rim	0.930	0.300	18.000	0.002	1.720	14.800	<0.0039	0.014	0.015	0.066	0.043	0.660	0.060	1.850	1.670	0.001	0.011	0.010	N.A.
A82-147 m	Py .1.4	Clast core	3.420	0.550	52.500	0.021	1.120	0.610	0.012	0.040	0.091	0.066	0.019	3.870	<0.500	1.900	1.770	<0.013	<0.008	<0.01	N.A.
Average			*1.121*	*0.246*	*21.440*	*0.091*	*59.110*	*68.353*	*0.278*	*1.396*	*0.040*	*0.035*	*0.028*	*10.558*	*0.085*	*1.188*	*1.765*	*0.025*	*0.009*	*0.023*	
A82-147 m	Py. 2.1	Clast	<0.0441	0.001	0.070	0.162	9.710	12.800	0.007	1.190	<0.01	0.000	0.038	280.000	1.860	0.500	1.680	0.051	0.370	<0.042	N.A.
A82-147 m	Py. 2.2	Clast	0.040	0.100	0.320	0.900	5.610	39.200	0.017	8.700	<0.036	0.003	0.083	107.000	2.800	0.600	1.940	0.024	0.223	<0.032	N.A.
A82-147 m	Py. 2.3	Clast	<0.0272	0.001	0.410	0.089	0.364	25.800	0.016	0.077	0.064	0.000	0.089	8.800	0.480	0.290	2.020	0.010	0.016	<0.026	N.A.
Average			*0.040*	*0.034*	*0.267*	*0.384*	*5.228*	*25.933*	*0.013*	*3.322*	*0.064*	*0.001*	*0.070*	*131.933*	*1.713*	*0.463*	*1.880*	*0.028*	*0.203*		
A82-147 m	Py. 3.2	Fine grained, in veinlet	0.920	0.390	9.700	67.000	7.600	7.900	10.230	1077.000	0.650	3.410	0.890	2770.000	43.400	15.200	1.790	0.219	1.240	0.594	N.A.
A82-147 m	Py. 3.3	Fine grained, in veinlet	1.780	0.630	3.620	136.400	9.470	14.600	2.960	269.800	0.510	4.260	0.360	1374.000	81.500	19.400	1.730	0.085	1.270	0.327	N.A.
Average			*1.350*	*0.510*	*6.660*	*101.700*	*8.535*	*11.250*	*6.595*	*673.400*	*0.580*	*3.835*	*0.625*	*2072.000*	*62.450*	*17.300*	*1.760*	*0.152*	*1.255*	*0.461*	

Abbreviations: Cv: covellite, Int2SE: analytical error, N.A.: not analyzed, Mcr: marcasite, Py: pyrite. Notes: The internal standard used was Fe for pyrite and marcasite (460000 ppm).

TABLE 1C

Selected trace element analyses of pyrite and marcasite determined by LA–ICPMS.

Average minimum detection limit (MDL) ppm			0.002	Int2SE	0.171	0.003	0.005	0.500	0.009	0.002	0.034	0.004	0.055	0.040	0.710	0.650	0.100	0.037	0.015	0.019	0.200
Epithermal stage. Heterolithic, matrix-supported hydrothermal breccia																					
Sample no.	**Analysis**	**Comments**	**Au (ppm)**	**Au ppm**	**As (ppm)**	**Ag (ppm)**	**Co (ppm)**	**Ni (ppm)**	**Pb (ppm)**	**Bi (ppm)**	**Te (ppm)**	**Mo (ppm)**	**V (ppm)**	**Cu (ppm)**	**Zn (ppm)**	**Mn (ppm)**	**Ge (ppm)**	**Cd (ppm)**	**Sn (ppm)**	**Sb (ppm)**	**Hg (ppm)**
AR82-160 m A	Py. 1.1	Rounded clast, core	<0.002	5.800	0.010	0.004	548.000	300.000	0.014	0.004	<0.034	<0.004	0.039	0.400	<0.71	0.230	1.190	0.020	<0.015	0.019	N.A.
AR82-160 m A	Py. 1.2	Rounded clast, core	<0.002	2.400	0.000	0.001	964.000	227.200	0.019	0.002	<0.034	<0.004	<0.055	0.640	<0.71	0.400	1.420	<0.037	0.017	<0.019	N.A.
AR82-160 m A	Py. 1.3	Rounded clast, core	0.003	18.000	0.090	0.001	32.570	435.000	0.008	0.002	<0.034	<0.004	<0.055	1.060	<0.71	<0.65	1.350	<0.037	<0.015	<0.019	N.A.
Average			*0.003*	*8.733*	*0.033*	*0.002*	*514.857*	*320.733*	*0.014*	*0.003*			*0.039*	*1.060*		*0.315*	*1.320*	*0.020*	*0.017*	*0.019*	
AR82-160 m A	Py. 2.1	Rounded clast, porous mid-section	0.048	5.200	0.180	0.038	0.250	0.230	0.440	0.481	0.137	0.004	<0.055	399.000	<0.71	0.900	1.550	0.016	<0.015	0.010	N.A.
AR82-160 m A	Py. 2.2	Rounded clast, porous mid-section	0.029	5.200	0.320	0.074	0.090	<0.50	1.360	0.415	0.128	<0.004	<0.055	413.000	<0.71	<0.65	1.400	<0.037	<0.015	0.035	N.A.
AR82-160 m A	Py. 2.3	Rounded clast, porous rim	0.036	12.000	0.630	3.630	57.800	357.000	2.590	2.760	0.210	<0.004	0.074	1191.000	<0.71	<0.65	1.250	<0.037	0.018	<0.019	N.A.
Average			*0.038*	*7.467*	*0.377*	*1.247*	*19.380*	*178.615*	*1.463*	*1.219*	*0.158*	*0.004*	*0.074*	*667.667*	*<0.71*	*0.900*	*1.400*	*0.016*	*0.018*	*0.023*	
AR82-160 m A	Py. 3.1	Anhedral clast, porous	0.033	4.400	0.340	1.245	4.000	21.500	3.770	9.330	1.390	<0.004	<0.055	1170.000	<0.71	0.740	1.310	0.023	<0.015	0.050	N.A.
AR82-160 m A	Py. 3.2	Anhedral clast, porous	0.069	1.000	0.870	1.900	16.400	70.100	8.890	4.520	0.230	<0.004	0.068	1209.000	1.640	1.080	1.250	0.017	0.019	0.009	N.A.
AR82-160 m A	Py. 3.3	Anhedral clast, porous	0.120	1.400	0.080	7.310	106.200	468.000	6.860	5.680	0.069	0.290	0.032	1429.000	<0.71	<0.65	1.270	<0.037	0.016	<0.019	N.A.
AR82-160 m A	Py. 3.4	Anhedral clast, porous	0.069	0.001	4.090	3.470	38.100	132.500	41.700	4.470	3.090	0.006	<0.055	1464.000	2.610	3.090	1.320	<0.037	0.070	0.059	N.A.
Average			*0.073*	*1.700*	*1.345*	*3.481*	*41.175*	*173.025*	*15.305*	*6.000*	*1.195*	*0.148*	*0.050*	*1318.000*	*2.125*	*1.637*	*1.288*	*0.020*	*0.035*	*0.039*	
AR82-160 m B	Py. 1.1	Anhedral clast in the breccia matrix	0.008	0.004	0.200	0.061	9.770	N.A.	N.A.	0.303	N.A.	0.007	0.045	194.000	7.000	N.A.	1.700	N.A.	0.070	0.000	N.A.
AR82-160 m B	Py. 1.2	Anhedral clast in the breccia matrix	0.001	0.001	0.980	0.002	84.400	N.A.	N.A.	0.002	N.A.	0.000	0.033	1.400	0.260	N.A.	1.670	N.A.	0.014	<0.0015	N.A.
AR82-160 m B	Py. 1.3	Anhedral clast in the breccia matrix	0.021	0.008	0.290	0.158	0.603	N.A.	N.A.	0.226	N.A.	0.000	0.039	410.000	<0.11	N.A.	1.730	N.A.	0.004	0.000	N.A.
AR82-160 m B	Py. 1.4	Anhedral clast in the breccia matrix	0.007	0.002	0.220	0.042	37.500	N.A.	N.A.	0.154	N.A.	0.000	0.058	19.700	<0.01	N.A.	1.640	N.A.	0.036	0.003	N.A.
AR82-160 m B	Py. 1.5	Anhedral clast in the breccia matrix	0.004	0.002	1.360	0.054	53.600	N.A.	N.A.	0.195	N.A.	0.000	0.059	8.700	0.720	N.A.	1.650	N.A.	0.036	0.004	N.A.
AR82-160 m B	Py. 1.6	Anhedral clast in the breccia matrix	0.029	0.008	0.720	0.440	65.800	N.A.	N.A.	0.870	N.A.	0.000	0.058	103.000	0.310	N.A.	1.450	N.A.	0.014	0.011	N.A.
AR82-160 m B	Py. 1.7	Anhedral clast in the breccia matrix	0.005	0.003	0.770	0.050	7.150	N.A.	N.A.	0.090	N.A.	0.103	0.277	91.000	21.000	N.A.	1.730	N.A.	0.085	0.014	N.A.
AR82-160 m B	Py. 1.8	Anhedral clast in the breccia matrix	0.000	0.000	0.430	0.004	29.000	N.A.	N.A.	0.051	N.A.	0.006	0.036	40.200	<0.23	N.A.	1.520	N.A.	0.023	0.002	N.A.
AR82-160 m B	Py. 1.9	Anhedral clast in the breccia matrix	0.000	0.001	<0.05	0.006	104.800	N.A.	N.A.	0.011	N.A.	0.000	0.030	3.800	0.330	N.A.	1.420	N.A.	0.012	0.000	N.A.
Average			*0.008*	*0.003*	*0.621*	*0.091*	*43.625*			*0.211*		*0.013*	*0.071*	*96.867*	*4.937*		*1.612*		*0.033*	*0.004*	
AR82-160.5 m	Py. 1.1	Subhedral, core	0.000	1.000	<0.51	0.035	66.400	4.000	0.001	0.160	0.019	0.004	0.066	19.500	0.290	0.200	1.260	<0.026	0.061	0.028	N.A.
AR82-160.5 m	Py. 1.2	Subhedral, core	0.000	1.000	0.000	0.009	86.800	3.400	0.000	0.033	<0.015	0.006	0.015	19.300	0.020	1.500	1.900	<0.012	0.014	0.021	N.A.
AR82-160.5 m	Py. 1.3	Subhedral, core	0.023	0.046	0.170	0.210	67.700	2.400	0.033	0.184	0.014	0.007	0.101	141.000	0.700	0.000	1.910	<0.008	0.030	0.023	N.A.
AR82-160.5 m	Py. 1.4	Subhedral, core	0.000	1.000	28.400	0.024	46.600	3.900	0.065	38.900	0.077	1.130	0.090	12.400	<0.15	1.100	1.520	<0.019	0.029	0.023	N.A.
Average			*0.006*	*0.762*	*9.523*	*0.070*	*66.875*	*3.425*	*0.025*	*9.819*	*0.037*	*0.287*	*0.068*	*48.050*	*0.337*	*0.700*	*1.648*		*0.034*	*0.024*	
AR82-160.5 m	Py. 2.1	Fine-grained, colloform, in veins	<0.0488	0.003	3.200	0.602	19.040	10.000	0.137	2.350	0.140	0.089	0.400	507.000	4.100	<0.2	1.410	0.070	6.800	3.700	N.A.
AR82-160.5 m	Py. 2.2	Fine-grained, colloform, in veins	0.053	0.087	1.220	1.580	9.400	13.700	0.288	1.960	0.003	0.036	0.104	54.300	1.100	0.600	2.020	0.017	0.190	0.084	N.A.
AR82-160.5 m	Py. 2.3	Fine-grained, colloform, in veins	0.013	0.060	<0.180	0.008	0.520	<0.01	0.000	0.074	<0.059	0.008	0.001	352.000	0.760	0.200	1.480	0.015	0.020	0.024	N.A.
AR82-160.5 m	Py. 2.4	Fine-grained, colloform, in veins	<0.0354	0.001	0.100	0.007	30.000	20.000	0.000	0.180	0.012	0.000	0.051	23.900	0.200	1.300	1.660	0.052	<0.005	0.018	N.A.
AR82-160.5 m	Py. 3.1	Fine-grained, colloform, in veins	0.400	0.260	0.420	0.041	7.320	5.200	0.020	0.630	0.024	0.000	3.020	145.000	2.000	1.200	1.580	0.028	0.470	0.120	N.A.
Average			*0.155*	*0.082*	*1.235*	*0.448*	*13.256*	*12.225*	*0.089*	*1.039*	*0.045*	*0.027*	*0.715*	*216.440*	*1.632*	*0.825*	*1.630*	*0.036*	*1.870*	*0.789*	

Abbreviations: Cv: covellite, Int2SE: analytical error, N.A.: not analyzed, Mcr: marcasite, Py: pyrite. Notes: The internal standard used was Fe for pyrite and marcasite (460000 ppm).

Table 1D
Selected trace element analyses of pyrite and marcasite determined by LA–ICPMS.

Average minimum detection limit (MDL) ppm			0.002	Int2SE	0.171	0.003	0.005	0.500	0.009	0.002	0.034	0.004	0.055	0.040	0.710	0.650	0.100	0.037	0.015	0.019	0.200
Epithermal stage. Clast-supported hydrothermal breccia																					
Sample no.	**Analysis**	**Comments**	**Au (ppm)**	**Au ppm**	**As (ppm)**	**Ag (ppm)**	**Co (ppm)**	**Ni (ppm)**	**Pb (ppm)**	**Bi (ppm)**	**Te (ppm)**	**Mo (ppm)**	**V (ppm)**	**Cu (ppm)**	**Zn (ppm)**	**Mn (ppm)**	**Ge (ppm)**	**Cd (ppm)**	**Sn (ppm)**	**Sb (ppm)**	**Hg (ppm)**
AR82-265 m	Py. 1.1	Euhedral to subhedral, fine-grained cement	0.021	0.009	0.170	0.171	105.000	51.500	1.160	1.920	0.036	0.003	0.012	277.000	2.400	0.510	1.530	<0.006	0.206	<0.003	N.A.
AR82-265 m	Py. 1.2	Euhedral to subhedral, fine-grained cement	0.028	0.007	<0.02	0.039	0.004	0.560	0.235	0.045	0.011	0.002	0.039	327.000	0.820	0.400	1.460	0.001	0.021	0.017	N.A.
AR82-265 m	Py. 1.3	Euhedral to subhedral, fine-grained cement	0.039	0.026	0.180	0.059	6.460	8.300	0.560	0.069	0.013	0.004	0.014	208.000	0.550	0.640	1.672	<0.008	0.013	0.001	N.A.
AR82-265 m	Py. 1.4	Euhedral to subhedral, fine-grained cement	0.040	0.051	0.130	0.052	44.900	708.000	0.420	0.103	0.000	0.000	0.140	62.000	4.200	0.460	1.410	0.031	0.060	<0.0508	N.A.
AR82-265 m	Py. 2.1	Euhedral to subhedral, fine-grained cement	0.031	0.006	0.120	0.179	81.200	332.000	0.605	0.277	0.019	0.000	0.230	270.000	3.200	0.480	1.405	0.005	0.097	<0.008	N.A.
AR82-265 m	Py. 2.2	Euhedral to subhedral, fine-grained cement	0.770	0.120	0.740	0.960	9.750	81.100	1.870	2.440	0.180	0.006	1.800	1076.000	2.200	0.690	4.260	0.025	0.780	0.094	N.A.
AR82-265 m	Py. 2.3	Euhedral to subhedral, fine-grained cement	0.008	0.003	8.730	0.042	554.000	57.700	1.010	0.338	1.240	0.117	0.057	41.000	0.270	0.380	1.380	0.005	0.006	0.017	N.A.
AR82-265 m	Py. 2.5	Euhedral to subhedral, fine-grained cement	0.001	0.001	0.080	0.036	92.100	42.600	0.044	0.006	0.000	0.000	0.046	82.900	0.200	0.440	1.350	0.001	0.005	<0.015	N.A.
AR82-265 m	Py. 2.6	Euhedral to subhedral, fine-grained cement	0.004	0.003	0.230	0.027	151.000	67.400	0.150	0.010	0.000	0.000	0.075	31.600	0.870	0.350	1.450	0.019	0.007	0.000	N.A.
Average			*0.105*	*0.025*	*1.298*	*0.174*	*116.046*	*149.907*	*0.673*	*0.579*	*0.167*	*0.015*	*0.268*	*263.944*	*1.634*	*0.483*	*1.769*	*0.012*	*0.133*	*0.026*	
Epithermal stage. Jigzaw hydrothermal breccia																					
AR82-359 m	Mcr. 2.1	Fine-grained anhedral rim	0.026	0.001	0.491	0.920	<0.005	<0.50	5.210	<0.002	0.513	<0.004	<0.055	7.050	0.121	<0.65	0.024	0.468	<0.015	0.031	N.A.
AR82-359 m	Mcr. 2.2	Fine-grained anhedral rim	0.051	0.001	0.663	1.657	0.079	0.356	8.310	0.005	1.021	<0.004	<0.055	18.740	0.159	<0.65	0.024	0.619	0.006	0.046	N.A.
AR82-359 m	Mcr. 2.3	Fine-grained anhedral rim	0.011	0.001	0.322	0.507	0.012	<0.50	9.540	0.004	0.208	<0.004	<0.055	1.720	4.530	0.714	0.026	0.345	0.013	<0.019	N.A.
AR82-359 m	Mcr. 2.4	Fine-grained anhedral rim	0.008	0.000	0.330	0.730	0.023	0.306	5.280	<0.002	0.143	<0.004	<0.055	1.705	5.356	0.671	0.025	0.310	0.006	<0.019	N.A.
Average			*0.024*	*0.001*	*0.451*	*0.954*	*0.038*	*0.331*	*7.085*	*0.004*	*0.471*	*<0.004*	*<0.055*	*7.304*	*2.541*	*0.693*	*0.025*	*0.436*	*0.008*	*0.039*	
AR82-359 m	Py. 1.1	Subhedral, core	0.000	0.001	0.150	0.021	9.370	20.400	0.025	0.003	0.010	0.000	<0.006	5.600	0.030	0.310	1.371	<0.0078	0.015	0.011	N.A.
AR82-359 m	Py. 1.2	Subhedral, core	0.000	0.001	<0.08	0.020	239.300	107.400	0.106	0.021	0.021	0.000	0.025	22.700	0.040	0.410	1.330	<0.00946	0.007	0.006	N.A.
AR82-359 m	Py. 1.3	Subhedral, core	0.000	0.001	0.120	0.019	84.900	122.600	0.015	0.003	0.000	0.000	<0.004	9.000	<0.07	0.260	1.567	<0.0043	0.016	<0.01	N.A.
AR82-359 m	Py. 1.4	Subhedral, core	0.002	0.001	<0.01	0.014	13.300	46.100	0.498	0.050	0.000	0.002	0.022	22.800	0.160	<0.04	1.240	0.004	0.001	<0.015	N.A.
Average			*0.000*	*0.001*	*0.135*	*0.019*	*86.718*	*74.125*	*0.161*	*0.019*	*0.008*	*0.001*	*0.024*	*15.025*	*0.077*	*0.327*	*1.377*	*0.004*	*0.010*	*0.009*	
AR82-359 m	Py. 3.1	Fine-grained enclosing Cv	0.011	0.004	<0.02	0.043	0.008	0.000	0.239	0.035	0.023	0.004	0.018	2961.000	0.070	0.580	1.380	0.000	0.033	0.022	N.A.
AR82-359 m	Py. 3.2	Fine-grained enclosing Cv	0.077	0.009	0.070	0.237	0.001	<0.17	0.290	0.441	0.045	0.006	0.014	2828.000	<0.16	<0.11	1.410	0.031	0.029	0.021	N.A.
AR82-359 m	Py. 3.3	Fine-grained enclosing Cv	0.016	0.004	1.020	5.960	0.007	0.200	235.000	0.041	0.067	0.132	0.022	2399.000	10.740	0.160	1.450	0.800	0.025	0.039	N.A.
Average			*0.035*	*0.006*	*0.545*	*2.080*	*0.005*	*0.100*	*78.510*	*0.172*	*0.045*	*0.047*	*0.018*	*2729.333*	*5.405*	*0.370*	*1.413*	*0.277*	*0.029*	*0.027*	

Abbreviations: Cv: covellite, Int2SE: analytical error, N.A.: not analyzed, Mcr: marcasite, Py: pyrite. Notes: The internal standard used was Fe for pyrite and marcasite (460000 ppm).

then petrographically. The composition of major and minor elements in sulfides was obtained using EMPA methods and has been reported in a previous study (Franchini et al., 2011). The microprobe analyses of individual pyrite grains confirmed that Fe and S concentrations do not deviate significantly from stoichiometric proportions. Based on these previous studies, 8 samples containing pyrite and marcasite were selected for laser ablation ICP-MS analyses (Fig. 1C).

Trace-element analyses ($n = 117$) and maps ($n = 36$) in pyrite and marcasite were performed at the LA–ICPMS laboratory of the Department of Earth Sciences of the University of New Brunswick, Canada (see McFarlane and Luo, 2012). The LA–ICPMS system used a Resonetics M-50 193 nm excimer laser system connected, via Nylon tubing, to an Agilent 7700x quadrupole ICP-MS equipped with dual external rotary pumps. The ICP-MS was operated at 1450 W and a torch depth of 5.0 mm and was tuned, while rastering across NIST610 glass, to achieve $ThO^+/Th^+ < 0.3\%$ (monitor of oxide production), $^{238}U^+/^{232}Th^+ \sim 1.0$ (monitor of plasma robustness), and $^{22}M^+/^{44}Ca^{++} < 0.3\%$ (monitor of double-charged production).

Samples and standards were loaded together into a two-volume low-volume Laurin Technic Pty sample cell that was repeatedly evacuated and backfilled with He to remove traces of air from the cell after each sample exchange. Sulfide samples were ablated in spot mode using 44 μm craters and a 4 Hz repetition with the laser energy (fluence) regulated at ~1.5 J/cm^2. Each point was ablated for 30 s following 40 s of gas background collection. For trace-element mapping, sulfides were ablated using a 17 μm crater, a stage scan speed of 8 μm/s and a 10 Hz repetition with the laser fluence regulated at ~1.5 J/cm^2. Ablated material was transported out of the two-volume low-volume ablation cell using 750 mL/min He as a carrier gas. This was mixed downstream of the cell with 2.5 mL/min N_2 (to enhance sensitivity) and 700 mL/min Ar (from the ICP-MS) prior to reaching the ICP-MS torch.

For spot analyses, the 'squid' smoothing device was used to ensure low %RSD signals; the 'squid' was removed for trace element mapping to ensure fastest possible washout from the cell (~3 orders of magnitude in 1 s). The following isotopes were analyzed in both modes of analysis: ^{29}Si, ^{34}S, ^{51}V, ^{55}Mn, ^{57}Fe, ^{59}Co, ^{60,62}Ni, ^{63}Cu, ^{66}Zn, ^{72}Ge, ^{75}As, ^{95}Mo, ^{107}Ag, ^{111}Cd, ^{118}Sn, ^{121}Sb, ^{125}Te, ^{197}Au, ^{207}Pb, ^{209}Bi, ^{125}Te, and ^{238}U. Analyte dwell times were set individually, with longest dwell times set for the lowest concentration elements. Total quadrupole sweep time was kept <0.5 s. Concentrations in unknowns were calibrated against sulfide reference material MASS-1 and an internal standard obtained by microprobe analyses: Fe for pyrite and marcasite. GSE-1 glass was used as a quality control standard. Replicate analyses of GSE-1G during each acquisition yielded relative deviations (%RD: $100 \times [(ppm_{meas} - ppm_{ref}) / ppm_{ref}]$) between ±25% with V, Mn, Co, Cu As, Mo, Ag, Cd, Sn, Pb, and Bi typically within 10% of the GEOREM reference values. Recovery of Au in GSE-1G was low (~3 ppm) compared to the reference value of 7 ppm. At the end of the ablation sequence, the laser log file and ICP-MS intensity data file were synchronized using Iolite™ (Paton et al., 2011) running as a plug in for Wave metrics Igor Pro 6.22™. Each ablation time-series was inspected offline and adjusted when necessary to avoid artifacts related to ablating through thin grains or from placement of craters overlapping other mineral (e.g., silicates). Spikes in the data were automatically filtered using the default 2σ outlier rejection in the Iolite internally- standardized trace-element data reduction scheme. For trace-element maps, non-pyrite material was masked using the Fe CPS elemental map as a guide; concentration scales for each map are shown as internally-standardized absolute ppm.

MASS-1 external standard has a somewhat inhomogeneous distribution of Au at the micron-scale. Thus, the gold concentration in sulfides and sulfosalts reported in this work should be viewed with some caution. Detection limits for analyses of Au varied for each run ranging from <0.001to 0.05 ppm. Limits of detection (LOD) are given in the supplementary data (Appendices A and B). In both Table 1 and in the appendices, results at ~1/2 the mean LOD were retained whereas those ≪LOD or with negative value are listed as <LOD. Special care was taken in the selection of pyrite free of inclusions. The analyzed samples do nevertheless show inhomogeneity, at least in some samples. Since the LA–ICPMS spot size is greater than many of these features, the ablation profiles will not always show homogeneity on the scale of the ablation spot. Representative single-spot spectra, showing both smooth and irregular profiles, were analyzed in pyrites enriched in trace elements. Abbreviations for minerals are from Whitney and Evans (2010).

5. Textural features of pyrite and marcasite

Pyrite is the most abundant sulfide at Agua Rica. Two main groups of pyrites were recognized: early crystals related to the porphyry stage and later pyrite related to the epithermal stage. Within each group, particularly at the epithermal stage, various pyrite generations were distinguished, based on differences in texture. Marcasite occurs in minor amounts in the hydrothermal breccias. Pyrite types and marcasite occurrence, their spatial relationship with alteration, geochemistry, and hydrothermal breccias can be seen in the cross-sections of Fig. 1C, D and in the drill hole AR82 of Fig. 2.

In the early porphyry stage, pyrite is the main sulfide in the potassic and phyllic alteration halos. It occurs as fine-grained disseminations (0.5 mm average) with hypogene chalcopyrite and traces of molybdenite and bornite in remnants of potassic alteration patches with hydrothermal biotite or K-feldspar in the Seca Norte porphyry. In the phyllic alteration envelope dominated by white micas + microcrystalline quartz aggregates + rutile and quartz stockwork veining, pyrite is accompanied by covellite + molybdenite. Pyrite textures vary from disseminations within phyllosilicate clots or within seams of phyllosilicates + rutile in the metasedimentary rocks, delineating phyllosilicate clots, filling hairline fractures and B-type quartz veinlets that crosscut the phyllic alteration assemblage. Pyrite occurring as subhedral to euhedral, very fine-grained crystals (0.04 to 0.15 mm) are always volumetrically more abundant than anhedral hypogene covellite and tabular molybdenite crystals. This pyrite contains vugs produced by the dissolution of micro-inclusions of sulfides (chalcopyrite, bornite, pyrrhotite).

In the epithermal stage, mineralization followed the formation of monolithic and heterolithic hydrothermal breccias. Pyrite occurs with other sulfides and advanced argillic mineral assemblages as hydrothermal cement in all breccia types and in clots and veinlets at depth in unbrecciated sectors of the Trampeadero porphyry and the metasedimentary rock. This breccia cement mineralization overprints the earlier phyllic alteration and an early and barren advanced argillic alteration. Some breccia clasts consist of polygranular pyrite (with subordinated covellite).

The hydrothermal breccias contain several epithermal pyrite generations. For example, in the jigsaw breccia (AR82, between 320 and 390 m depth; Fig. 2), pyrite fills the open space between clasts, the fractures within clasts, and early reopened quartz veins with the assemblage covellite + enargite ± molybdenite ± kuramite and marcasite accompanied by alunite + diaspore + native sulfur. Euhedral pyrite (0.1 to 1 mm) rims covellite (Fig. 3A) and contains inclusions of kuramite, zunyite, diaspore, and relict quartz (Fig. 3B, D). A few crystals are rimmed by a second pyrite generation (Fig. 3C) and anhedral or radiating marcasite (Fig. 3D). At approximately 290 m depth, beneath a zone of intense faulting, the hydrothermal breccia becomes mainly clast supported (Fig. 2) and epithermal pyrite occurs with covellite ± enargite ± molybdenite ± kuramite, and marcasite accompanied by alunite and alumino-phosphate-sulfates (APS) ± diaspore ± zunyite ± native sulfur ± rutile or anatase as hydrothermal cement. Pyrite occurs as idiomorphic to subidiomorphic, fine-grained (0.25 to 1 mm) crystals with morphologies dominated by pentagonal dodecahedra and subordinate octahedra. The crystals contain micro-inclusions and irregular boundaries alternate with crystal faces. Marcasite occurs in minor

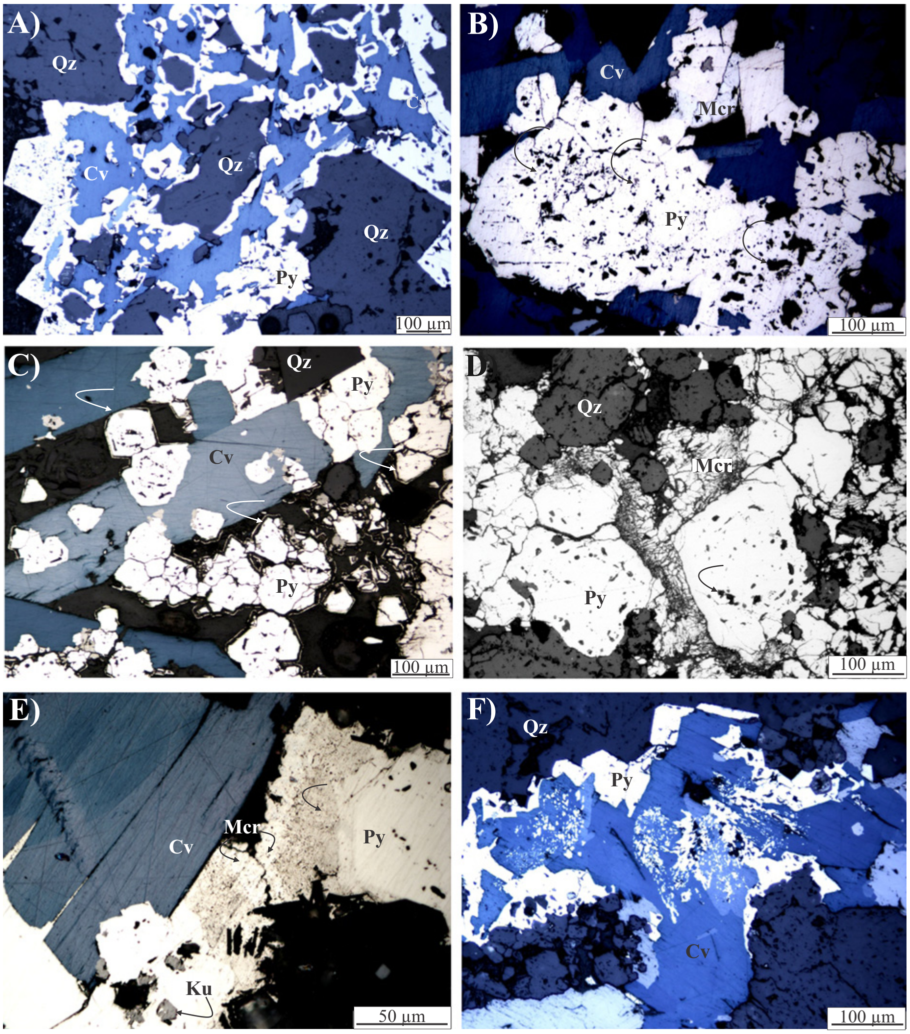

Fig. 3. Reflected light microphotographs illustrating the textures of pyrite (Py) in the hydrothermal breccias between 390 and 248 m depth. A) Euhedral pyrite (0.1 to 1 mm) rims covellite (Cv). B) Micro-inclusions in pyrite, some filled with kuramite, others with zunyite, diaspore and relict quartz (arrows); interstitial marcasite (Mcr) between pyrite crystals. C) Pyrite rimmed by a second pyrite generation. D) Marcasite rimming pyrite. E) Thin band of very fine-grained and brownish pyrite separating pyrite and marcasite (arrow); kuramite (Ku) inclusions in pyrite. F) Micro-inclusions of remnants pyrite in covellite. Qz: quartz.

amounts as radiating laths (0.05 mm) filling interstices between pyrite and covellite and plates of covellite, and rims pyrite crystals. There is usually a thin band of very fine-grained, brownish pyrite separating pyrite and marcasite (Fig. 3E). At 267 m depth, the covellite cement of the breccia contains numerous micro-inclusions of remnant pyrite (Fig. 3F). Another breccia sample (AR82-259 m; Fig. 2) contains pyrite as small and very porous (formed by micro-scale inclusions that have been plucked, resulting in a pseudo-porous texture) crystals and as big and euhedral crystals that include probably remobilized molybdenite. Veinlets of pyrite and alunite (AR82-248 m; Fig. 2) cut the altered porphyry clasts in the breccia.

In the matrix-supported heterolithic hydrothermal breccia (AR82 between 140 and 170 m depth; Fig. 2), early pyrite cores are rimmed by at least two generations of epithermal pyrite bands (Fig. 4A). The anhedral (rounded to subrounded) coarse-grained pyrite is overgrown (mantled) by a much finer grained, crudely colloform to sieve-textured pyrite (locally very fine grained; Fig. 4B, C). Some cores contain micro-scale to minute inclusions of rounded rutile, chalcopyrite–bornite or pyrrhotite; note some of this is plucked as well (pseudo-porous texture; Fig. 4D). The colloform pyrite also fills vugs in the early pyrite cores where they form micro-geodes up to 60 µm in diameter with pyrite grains protruding into vugs (Fig. 4E). Colloform pyrite is locally disseminated as cement of the breccias and fills seams and veinlets (Fig. 4F). Emplectite and sphalerite (AR82-160 m) rim pyrite and aikinite fill voids of the breccia. At 147 m depth, a late alunite veinlet has been reopened and filled with very fine-grained pyrite (0.005–0.01 mm; Fig. 4G).

In the upper levels of the matrix-supported hydrothermal breccia (AR82-96 m depth; Fig. 2), an early pyrite in sub-rounded crystal aggregates with interstitial covellite occurs as breccia clasts and as anhedral grains in the clastic matrix with pyrophyllite, zunyite, covellite, rutile or anatase, and native sulfur. Late colloform pyrite occurs as a rim of early crystals and as very fine-grained spherulites intergrown with sphalerite cementing the breccia clasts, replacing the matrix, and filling veinlets that cut the breccia. In other sectors of the same breccias, fine-grained marcasite with sphalerite and alunite constitute late cements (Fig. 4H).

East of the main central breccia, pyrite occurs in the monolithic Trampeadero and metasedimentary breccias as cement with covellite + diaspore ± zunyite and alunite + zunyite ± enargite, respectively. It also occurs in veinlets and clots in sectors of the Trampeadero porphyry with covellite ± diaspore ± alunite ± native sulfur (between 17 and

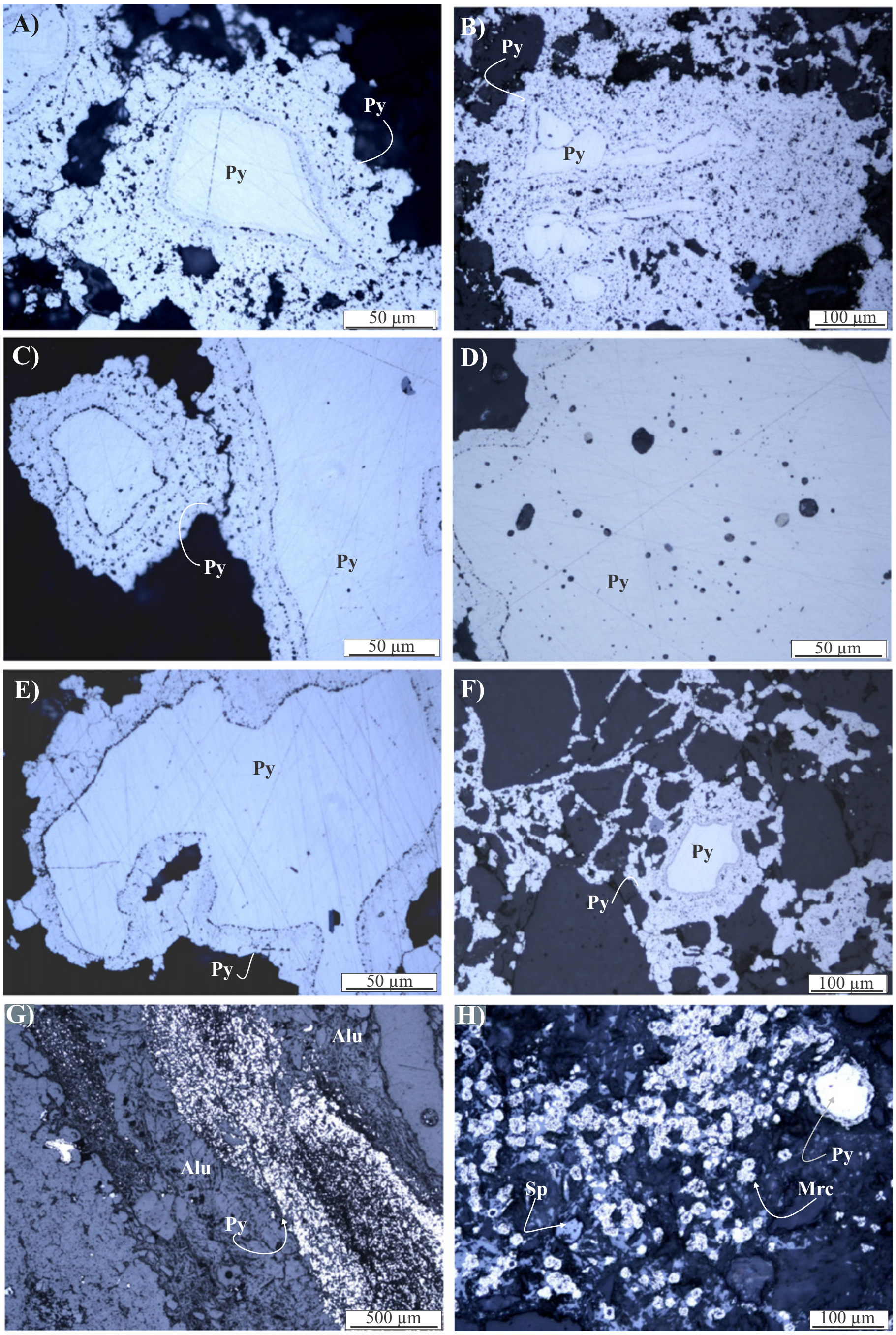

Fig. 4. Reflected light microphotographs illustrating the textures of pyrite in the hydrothermal breccias between 170 and 96 m depth (Fig. 2). A to C) Early pyrite (Py) cores are rimmed by colloform to sieve-textured pyrite bands (locally very fine grained). D) Micro-scale inclusions of rounded rutile, chalcopyrite–bornite or pyrrhotite; note some of this is plucked as well (pseudo-porous texture). E) Micro-geodes of colloform pyrite fill vugs in the early pyrite cores. F) Seams, veinlets, and cement of colloform pyrite. G) Reopened alunite (Alu) veinlet filled with very fine-grained pyrite (0.005–0.0 mm). H) Late, fine-grained spherulites of marcasite (Mcr) and sphalerite (Sp) rim pyrite clasts and cemented the breccia.

77 m depth and at 266 m depth) overprinting the phyllic alteration and the transitional alteration with andalusite (Fig. 1C).

6. Trace element composition

1. Porphyry stage pyrite

The fine-grained pyrite grains from the porphyry stage are, in general (except for Co and Ni; Table 1), trace-metal poor (sample AR9-187 m; Fig. 1C; Table 1), with the exception of pyrite from an early quartz vein that contains traces of As (up to 2.70 ppm) and Cu (87 ppm; AR18-85 m, Fig. 1C; Table 1). This vein has chalcopyrite partially replaced by covellite and a halo of alunite.

2. Epithermal stage pyrite

In the jig-saw breccia (AR82-359 m depth; Fig. 2), euhedral pyrite that rims covellite is significantly enriched in Cu (up to 2961 ppm) and depleted in Co (<0.008 ppm) and Ni (<0.2 ppm) compared to the subhedral crystals inherited from the porphyry stage (up to 239.3 ppm Co and 122.6 ppm Ni; Table 1). Some of these early crystals are rimmed by marcasite.

Pyrite grains in the cement of the clast-supported hydrothermal breccia (AR82-265 m; Fig. 2) are slightly enriched in all elements compared to the early pyrite from the porphyry stage (Table 1). Nine spots in different euhedral, corroded, and fine-grained pyrite associated with covellite were analyzed. This group shows a high correspondence between Au and V, Sn, Ge, Cu, Ag, and Sb, and a weak covariation or absence of any trend with the rest of the analyzed trace elements (Fig. 5). A representative time-resolved LA–ICPMS signal of a pyrite grain from this zone is shown in Fig. 6. Elemental concentrations for major components are stable (e.g., Fe and S) and trace element concentrations are generally low, with the exception of the high (but heterogeneous) Cu distribution (Table 1). Some optically homogeneous pyrite grains show transient signals indicating the presence of micro-inclusions (Fig. 6). Such inclusions contain Cu as a major component and additionally have concentrations of Bi, Zn, Pb, Ag, Au, and Sn that are highly variable, as indicated by imperfect covariation of Cu with other trace metals even within one pyrite host (Fig. 6A, B, C). Another LA–ICPMS spectra for this pyrite shows characteristically spikey signals for V and Sn (Fig. 6D), and an elevated but smooth Cu signal that can be correlated with Fe and S and interpreted as micro-inclusions of Cu–Fe sulfides.

Fig. 7 shows LA–ICPMS trace element maps of a selected pyrite grain. Pyrite shows a noticeable zonation that includes a Co-rich core followed by a band-like enrichment of Cu in the mid-section, whereas Zn and Au are enriched towards the rim. High values of As, Sn, Cu, V, Sb, Mo, and Bi are concentrated in the upper right zone of the grain towards the rim (Fig. 7), and in small spots as seen from the color intensity in the images. Some Ag and Bi are observed in the rims, and high-intensity Au spots suggest the presence of Au-bearing "invisible" micro- to nano-scale inclusions.

Five types of pyrite were analyzed in the heterolithic matrix-supported hydrothermal breccia (AR82-160, 160.5 m depth, Fig. 2): a large, internally zoned subhedral clast, small anhedral clasts with sieve-like texture, fine-grained and anhedral pyrite grain from the matrix, and fine-grained pyrite in a veinlet. Spot analyses conducted in the zoned clast (Table 1) show a massive core surrounded by colloform rims enriched in Cu, Pb, Bi, Ag, As, Te, and Au, with respect to the core. The anhedral and sieve-like pyrite clasts show the highest Cu (up to

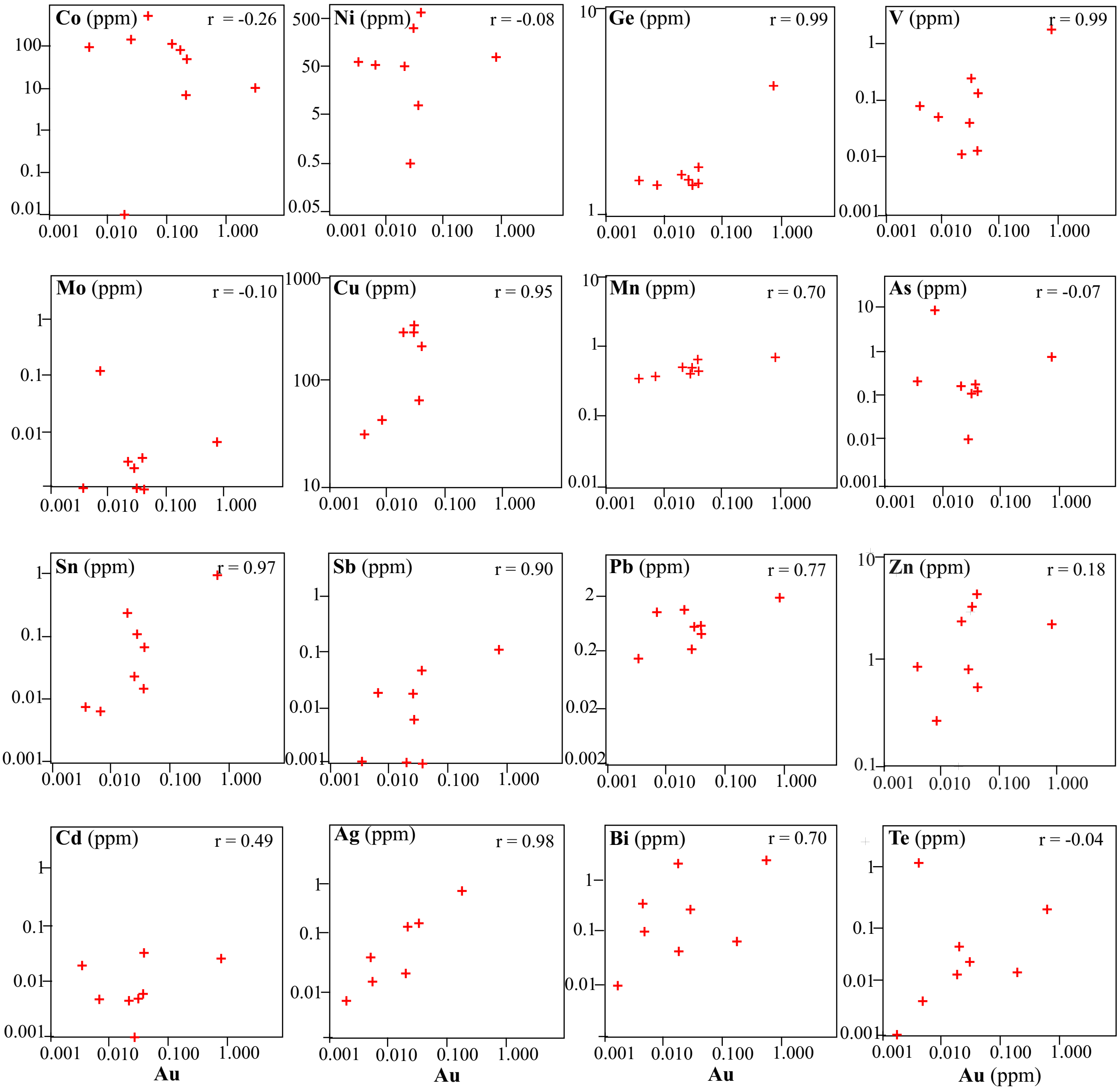

Fig. 5. Binary plots of selected trace elements (all in ppm) for pyrite analysis from the clast-supported hydrothermal breccia (AR82-265 m depth). Pearson correlation coefficients are displayed with each binary plot.

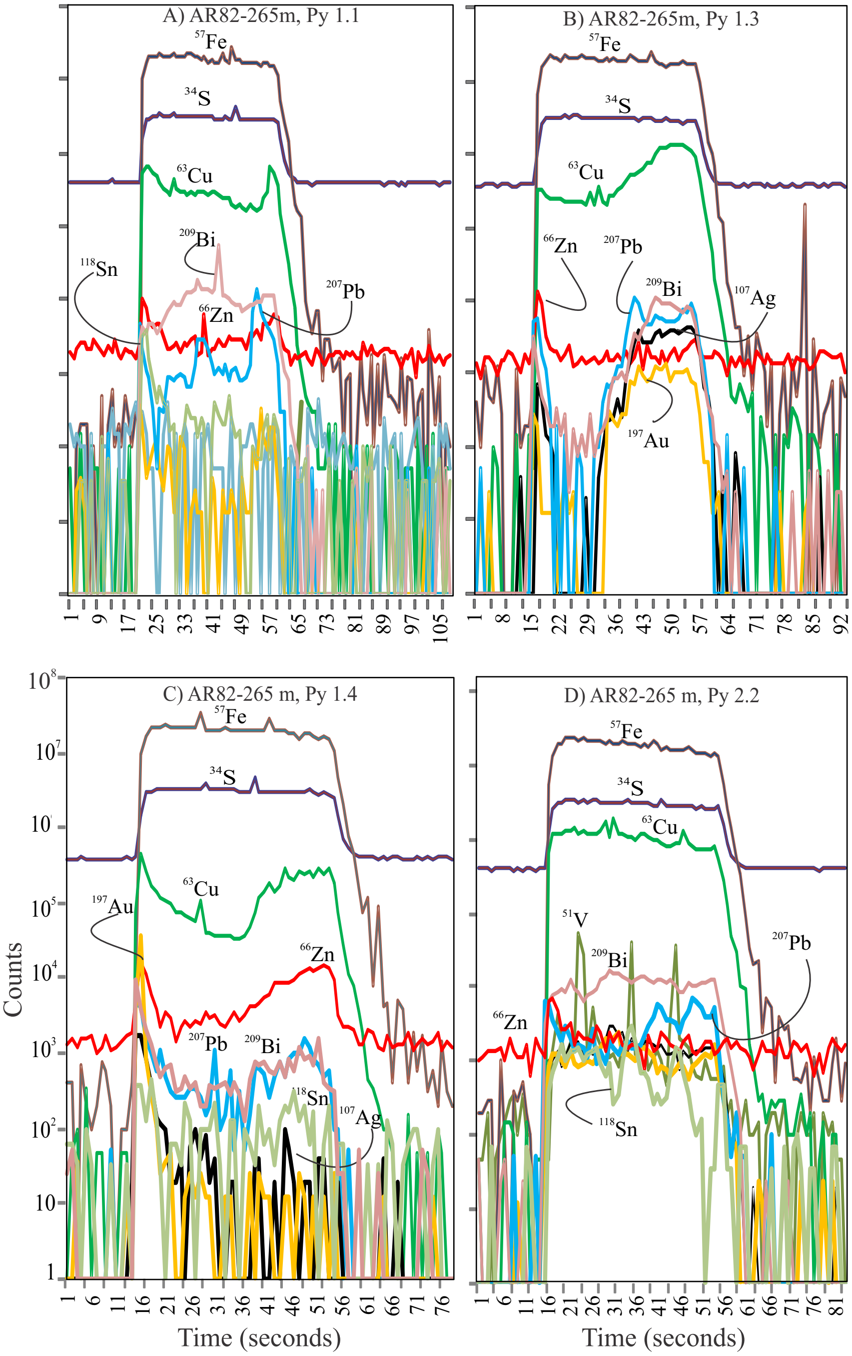

Fig. 6. Representative single-spot LA–ICPMS spectra for selected elements in pyrite from sample AR82-265 m. A) Spot 1.1. Note the general smooth and parallel signals for Fe and S and numerous spikes in the signal for Cu, Bi, Pb, Zn, and Sn. B) Spot 1.3. High signals of Cu, Bi, Pb, Ag, and Au as the crater intercepts a sulfosalt inclusions. C) Spot 1.4. A similar trend of Cu, Ag, Zn, Bi, and Au enrichment is seen in the edge of the grain. D) Spot 2.2. Another characteristic spikey signal for V and Sn that do not correlated with small peaks for Pb and Zn; Cu and Bi shows a relatively smooth signal.

1464 ppm), Pb (41.7 ppm), Ag (up to 7.3 ppm), Bi (9.3 ppm), and Te (3.1 ppm) contents of all analyzed pyrite grains in this sample and the fine-grained pyrite from the veinlet has the highest Au content (up to 0.40 ppm) followed by anhedral clast of pyrite (0.12 ppm). In general, Au shows a relatively good correspondence with Ag and Cu, but no significant covariation with the rest of the analyzed elements.

The best examples of zoned pyrite crystals are samples of the heterolithic breccia from 146 and 147 m depths. In these breccia samples, pyrite in the clasts (and as elongated crystals from a stringer) is rimmed by late, irregular, colloform pyrite overgrowths. Locally, a thin band of early pyrite occurs between bands of the late (colloform) pyrite. Spot analyses conducted on three pyrite generations (Table 1) show that the colloform bands in the crystal are enriched in Pb (up to 4190 ppm), Cu (up to 3900 ppm), Zn (up to 1045 ppm), Au (up to 6.7 ppm), Ag (up to 122 ppm), Bi (up to 184 ppm), and Te (up to 2.3 ppm). Gold shows a clear positive correlation ($r > 0.95$) with increased As, Pb, Mn, Ag, Bi, and Sb, although no correspondence is observed between Au and Co, Mo, Ni, and Ge ($r \approx 0$; Fig. 8).

Representative single-spot LA–ICPMS spectra for selected elements in the second generation of colloform pyrite show high concentrations of Cu and Pb, enrichment in Bi, Zn, Ag, and minor Au and As. These elements show variable concentrations with increasing crater depth and

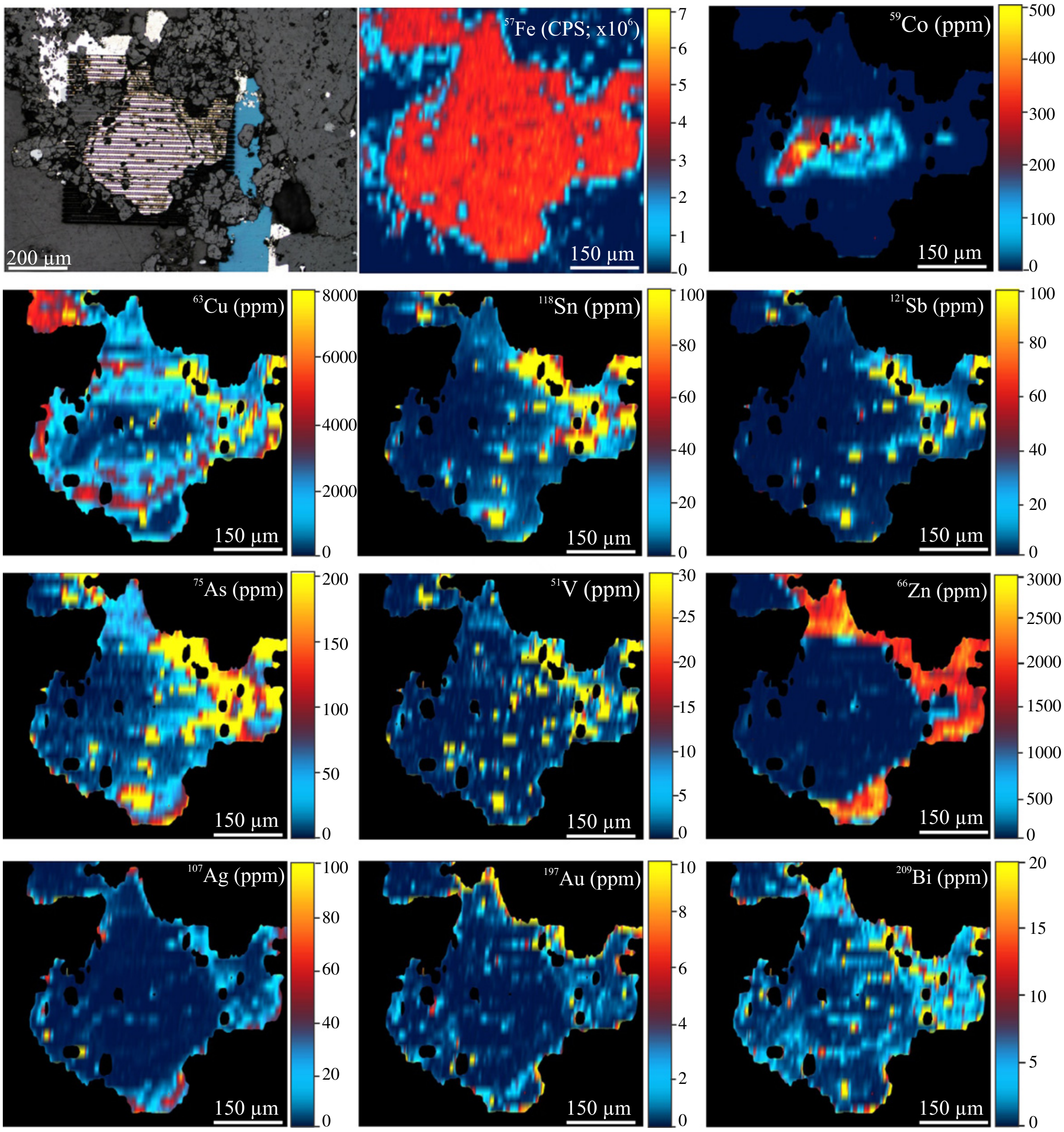

Fig. 7. LA–ICP-MS mapping of trace elements distribution (in ppm) in a zoned pyrite crystal from sample AR82-265 m (clast-supported hydrothermal breccia) with a Co-rich core, a Cu-rich mid-section, and a rim enriched in Zn, Ag, Bi, and Au. A micro-inclusion enriched in Cu, V, Sn, As, Sb, Si, and Bi occurs in the upper right sector of the crystal rim. CPS: counts per second. The first picture shows a reflected light microphotograph of the analyzed pyrite crystal.

show very small irregularities (Fig. 9A), with the exception of Bi, Ag, and Zn peaks in spots7.3 and 10.3 (Fig. 9B, C). A very good correspondence between the Bi and Ag peaks is evident. In the third generation of colloform pyrite, these same elements display higher variance and ragged profiles with good correspondence between Bi and Ag, and only subtle trending relations between Zn, Ag, and Au, between Au and Ag, and between Pb, Cu, Bi, and Au (Fig. 9D, E). Notable and elevated Pb and Cu contents (w/r to Fe and S) are observed in the rim of another pyrite crystal, as well as relatively smooth and parallel profiles for most elements (Fig. 9G). Pyrite in the stringers is enriched in Pb (up to 4528 ppm), Cu (up to 2270 ppm), Zn (up to 1078 ppm), Bi (up to 80 ppm), Au (up to 4 ppm), As (up to 25.2 ppm), Ag (up to 80.8 ppm), Te (up to 2.7 ppm), Mn (up to 96.7 ppm), Cd (up to 5.2 ppm), and <1 ppm Sb and Sn (Table 1).

The LA–ICPMS mapping presented in Fig. 10 shows a zoned pyrite crystal (sample AR82-146 m; Fig. 2) with a mid-section of the early pyrite generation enriched in Co, followed by a thin band rich in As, Cu, Au, Ag, Bi and a rim enriched in Cu, Au, Ag, Bi, and Zn, both the banding and the rim are part of the late colloform pyrite. Vanadium, Sb, and Sn are not associated with any of the aforementioned metals and they are mainly concentrated as scattered small inclusions within pyrite, showing a good correspondence between them. Another zoned pyrite crystal from the same sample (Fig. 11) shows similar trace-element enrichment and distribution, except for V, Sn, and Sb that are also slightly enriched in the crystal rim.

In sample AR82-147 m (Fig. 2), very fine-grained anhedral pyrite crystals from a late veinlet that cut the breccia have the highest Bi content of all analyzed pyrite in this study (up to 1077 ppm). Such high Bi values are in agreement with enrichment in Cu, Ag, Au, Mo, Zn, Mn, Sb, Sn, and V, compared to the early, subhedral pyrite grains from the matrix and clasts of the breccia (most analyses <10 ppm; Table 1).

The pyrite grains from the shallower sections of the deposit come from a similar heterolithic hydrothermal breccia sample (AR82-96 m; Fig. 2) that contains late marcasite, colloform pyrite, and

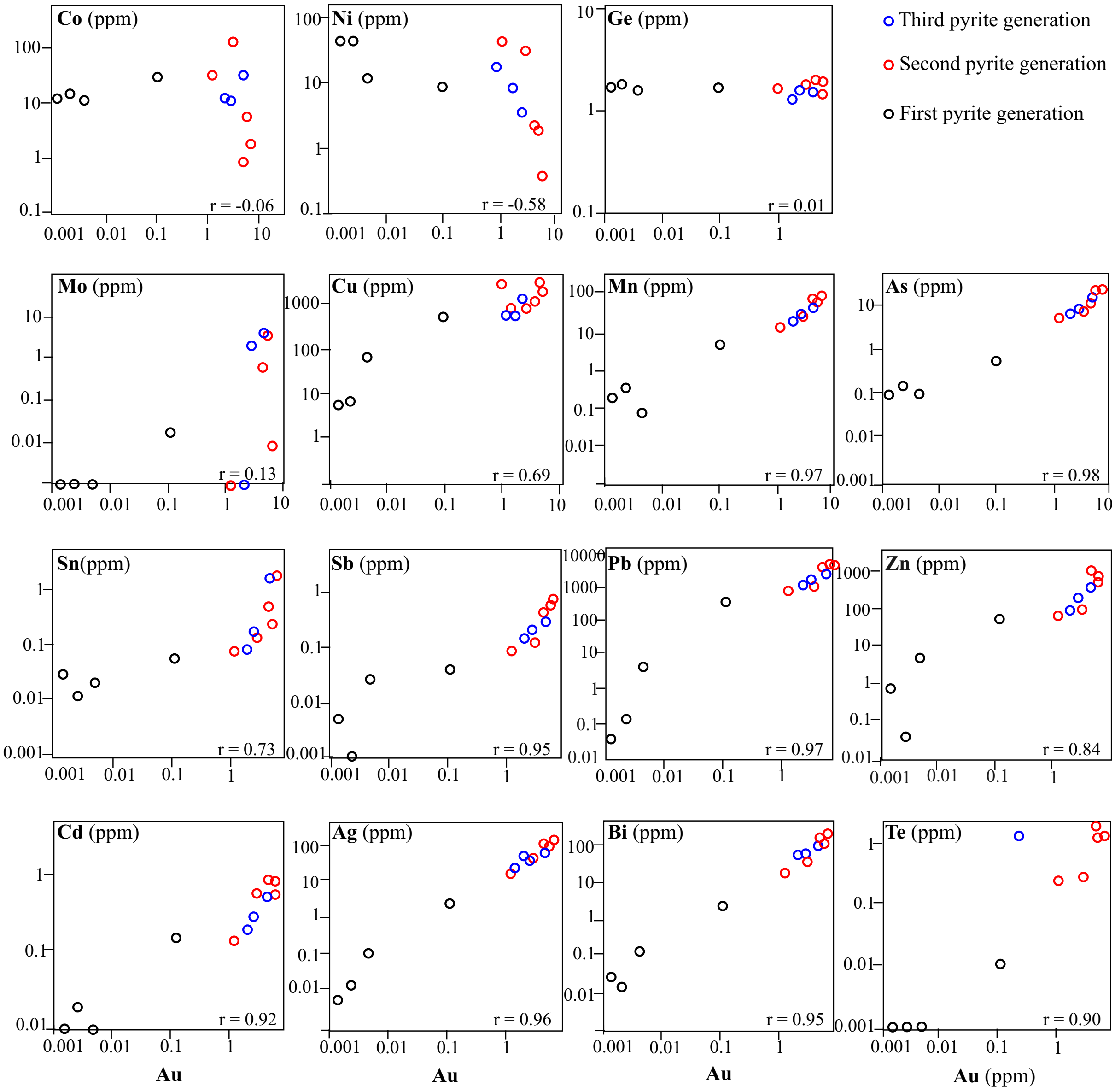

Fig. 8. Binary plots of selected trace elements (in ppm) for colloform pyrite analysis from the matrix-supported hydrothermal breccias (AR82-146 m depth). Pearson correlation coefficients are displayed with each binary plot.

sphalerite. Spot analyses conducted on a pyrite clast, fragments of pyrite in the matrix, and fine-grained marcasite cement, show that the latter is enriched in Zn, Cu, Pb, Ag, Bi, Au, Sn, Sb, and Cd, when compared to the earlier generations of pyrite (Table 1). In addition, it has the highest Zn contents (up to 59,000 ppm) that correspond with the highest Cd (up to 27.3 ppm) and Ag (up to 940 ppm) contents of all analysis, although such high Zn (and Cd) could be due to the fine-grained nature of marcasite, which is in direct contact with sphalerite.

7. Discussion

In a previous study, Franchini et al. (2011) reported EMPA analyses of pyrite from Agua Rica showing elemental enrichment in zoned grains from the breccias, including rims slightly enriched in Zn, Cu, As, Sb, and Ag relative to the pyrite cores. When our new LA–ICPMS spot analyses are combined with quantitative elemental maps (Section 6), it is possible to constrain whether a particular trace element occurs as a homogeneous substituent or as micro- to nano-sized inclusions, or alternatively, as larger isolated micron-sized inclusions within pyrite. It is noteworthy to mention that a finer distinction between nanoparticulate versus solid solution incorporation of metals was not possible to determine exclusively using LA–ICPMS data, but is later constrained for Au using Au–As relations (Reich et al., 2013).

7.1. Trace elements in pyrite and textures as indicators of the porphyry to epithermal transition

We recognize compositional and textural variations of pyrite grains precipitated in the porphyry stage and at various phases of the evolution of the high sulfidation epithermal mineralization process at Agua Rica. In general, pyrite crystals from the porphyry stage are fine grained (0. 04 to 0.5 mm) and trace element-poor (Table 1). Few studies have documented the mineralogy and trace element composition of pyrite in high-temperature porphyry deposits. For example, at the Pebble porphyry Cu–Au–Mo deposit, pyrite in the sodic–potassic and potassic assemblages contains high copper (0.47–14.0 ppm), Co (up to 2031 ppm), Ni (up to 5827 ppm), and up to 4.3 ppm Au (Gregory et al., 2013). A recent SIMS/EMPA study at the Dexing porphyry Cu (Mo–Au) deposit in China shows that Cu, As, Au, and Ni are the most

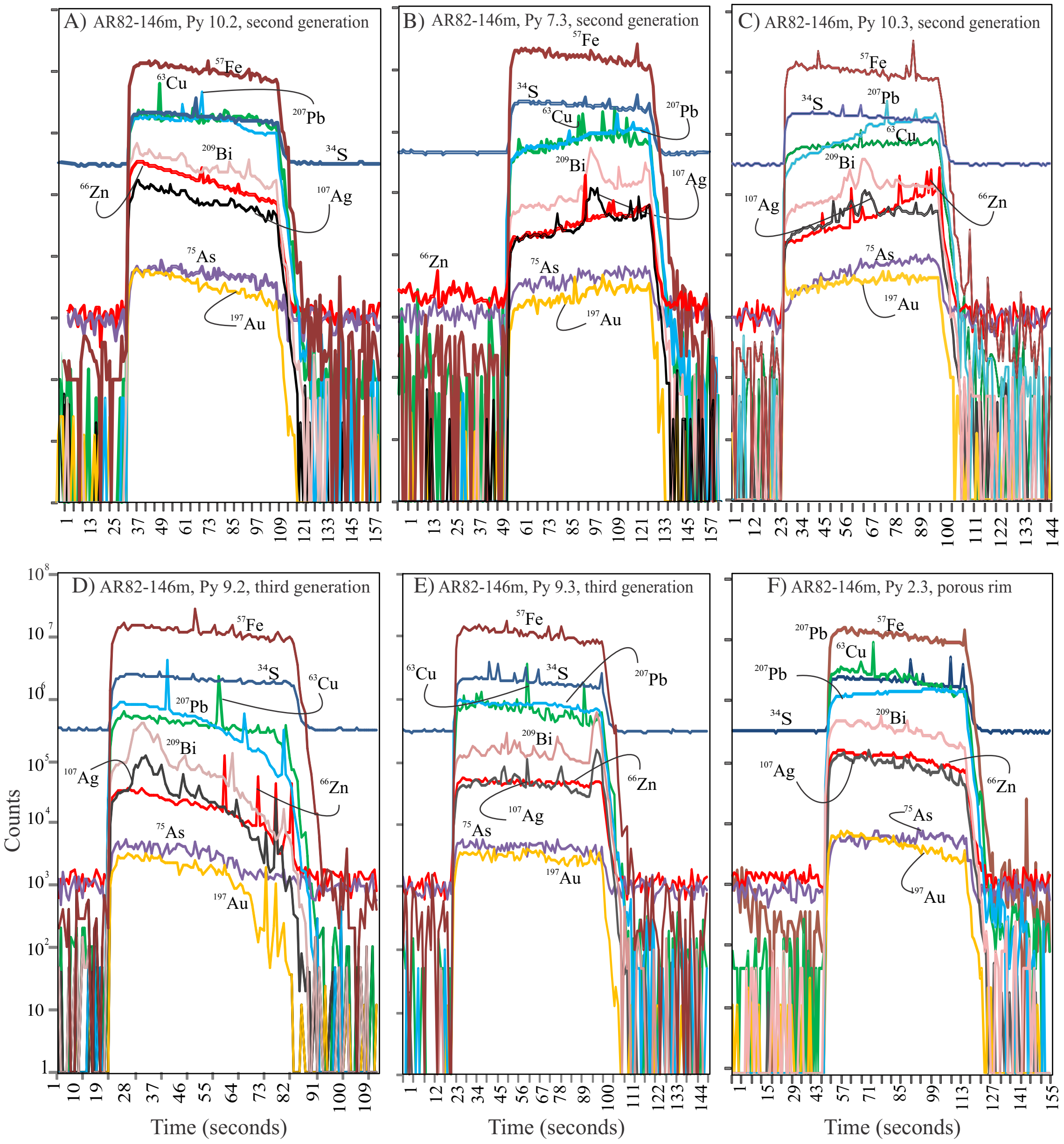

Fig. 9. Representative single-spot LA–ICPMS spectra for selected elements in the second and third colloform pyrite generations from sample AR82-146 m (Fig. 2). Note high concentrations of Cu and Pb in all profiles. A) Very small peaks of Cu and Pb and a decrease of Bi, Zn, Ag, and Au with increasing crater depth. B–C) Increase in Pb, Bi, Ag, and Zn with crater depth; note good correlation between peaks of Bi and Ag. D–E) These same elements display higher variance and ragged profiles with good correlations between Bi and Ag, Ag, and Au. G) High Pb and Cu contents in the spot of the colloform pyrite rim and the relatively smooth and parallel profiles of most elements.

abundant elements in pyrite with concentrations that vary from sub-ppm levels to a few wt.% (i.e., ~6 wt.% Cu, ~3 wt.% As, ~0.25 wt.% Au, and ~0.2 wt.% Ni) (Reich et al., 2013). Detailed EMPA and WDS mapping of the Dexing pyrites revealed complex zoning where Cu, Au, and As occur in different mineralogical forms. For example, Cu and Au can occur as solid solution in pyrite, as well as encapsulated forming micro- to nano-scale metal sulfides, such as chalcopyrite and native Au (Reich et al., 2013). At the Altar porphyry Cu (Au–Mo) deposit, a significant fraction of gold of the early stockwork veins occurs in pyrite as submicroscopic particles that are spatially related to inclusions of a Bi–Te–Pb–Ag-enriched Cu–Fe-sulfide phase (Zwahlen et al., 2014). In this deposit, Maydagán et al. (2013) found low contents of trace elements in pyrite from the potassic stage but documented the presence of micro- to nano-scale sized Au (Ag alloys) and sulfosalt inclusions with As, Ag, V, Zn, Sn, Bi, and Sb in pyrite from the phyllic stage.

At Agua Rica, a preliminary analysis of metal speciation in pyrite, based on the methodology by Reich et al. (2005), indicates that Au is present in both mineralogical forms (solid solution as Au^{+1} and native as Au^0). Fig. 12 shows Au–As relations of pyrite from porphyry and epithermal deposits as reported by Deditius et al. (2014) (red and yellow fields). In this diagram, the solubility limit of Au as a function of As (red segmented line) separates the Au–As space in two fields, where high Au/As ratios indicate speciation of Au in pyrite as native Au nanoparticles (NPs, above the red line) while low Au/As ratios are indicative of solid solution incorporation (SS, below the line). At Agua Rica, most pyrite samples from the porphyry stage, jigsaw hydrothermal breccia, clast-supported hydrothermal breccia, and matrix-

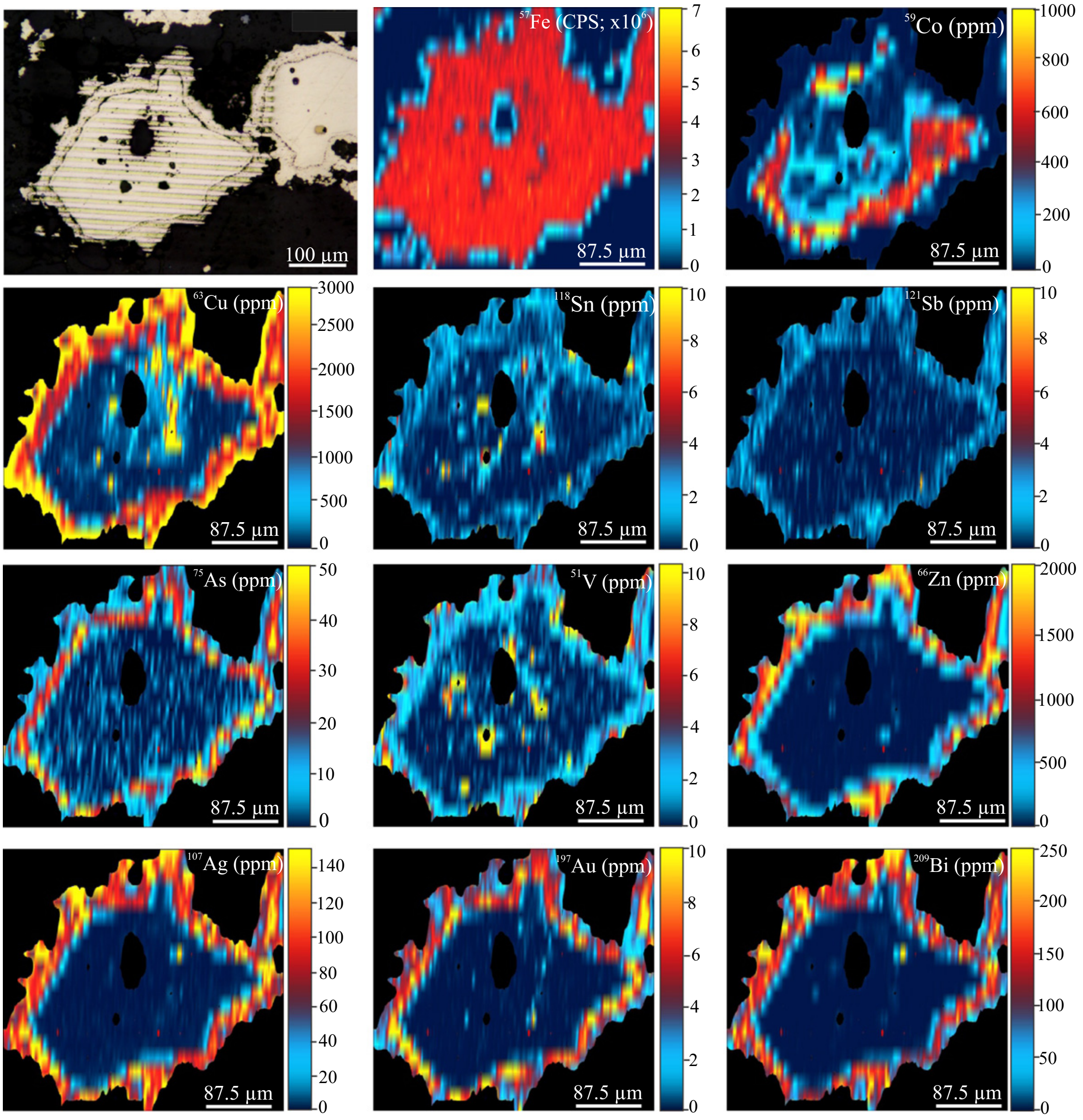

Fig. 10. LA–ICP-MS mapping of trace elements distribution (in ppm) in a zoned pyrite crystal from sample AR82-146 m (Fig. 2) with a core enriched in Co and minor Mo, and colloform bands rich in As, Cu, Au, Ag, Bi, and Zn. Note scattered small inclusions rich in V, Sb, and Sn. CPS: counts per second. The first picture shows a reflected light microphotograph of the analyzed pyrite crystal.

supported hydrothermal breccia (pyrite clasts), plot below the Au solubility line suggesting solid solution incorporation (Fig. 12). In contrast, most samples of the late, colloform pyrite plot above the solubility limit at high Au/As, indicating that most of their measured Au is contained as nanoparticles of native Au.

The previous analysis is consistent with a view where Au and other trace elements in the early pyrites from the porphyry stage may have been leached and remobilized during later mineralization stages related to the advanced argillic overprint. Pyrite crystals that precipitated during the high sulfidation mineralization stage are texturally complex and have significantly more elevated concentrations of trace elements including Pb, Ag, Zn, Sb, Bi, Cu, and Au (Table 1). Therefore, it is likely that metals leached from early pyrites (porphyry stage) may have contributed to the metal budget of late epithermal fluids that precipitated trace metals as submicron-sized particles within newly formed colloform pyrites after cooling and super saturation. The trace element budget of pyrites at Agua Rica vary with depth and within sub-stages of mineralization, and results from this study show a correspondence between the trace-metal content of pyrite and the ore grades of the host rock. For example, in the jigsaw hydrothermal breccia with the highest grades of Cu (up to 3.7 % Cu; Fig. 2), euhedral pyrite crystals are enriched in Cu (up to 2961). At shallower levels (10 to 196 m depth), in the heterolithic hydrothermal breccia (0.6 % Cu) with the highest grades of Zn (up to 0.55 %), Pb (up to 0.53 %), Au (up to 5.6 g/t), and Ag (up to 325 g/t) (Fig. 2) late, colloform pyrite is enriched in Pb (up to 4528 ppm), Cu (up to 3900 ppm), Zn (up to 1078 ppm), Ag (up to 136 ppm), Au (up to 6.7 ppm), and Bi (up to1077 ppm). This suggests that variations in the trace element contents and textures in pyrite corresponding to different hydrothermal mineralization stages in a complex system like Agua Rica, may serve as vectors to ore in exploration.

7.2. Variations in trace elements and textures of epithermal pyrite

Pyrite from the epithermal breccias at intermediate depths occur as idiomorphic to subidiomorphic, coarser grained (up to 1 mm) crystals

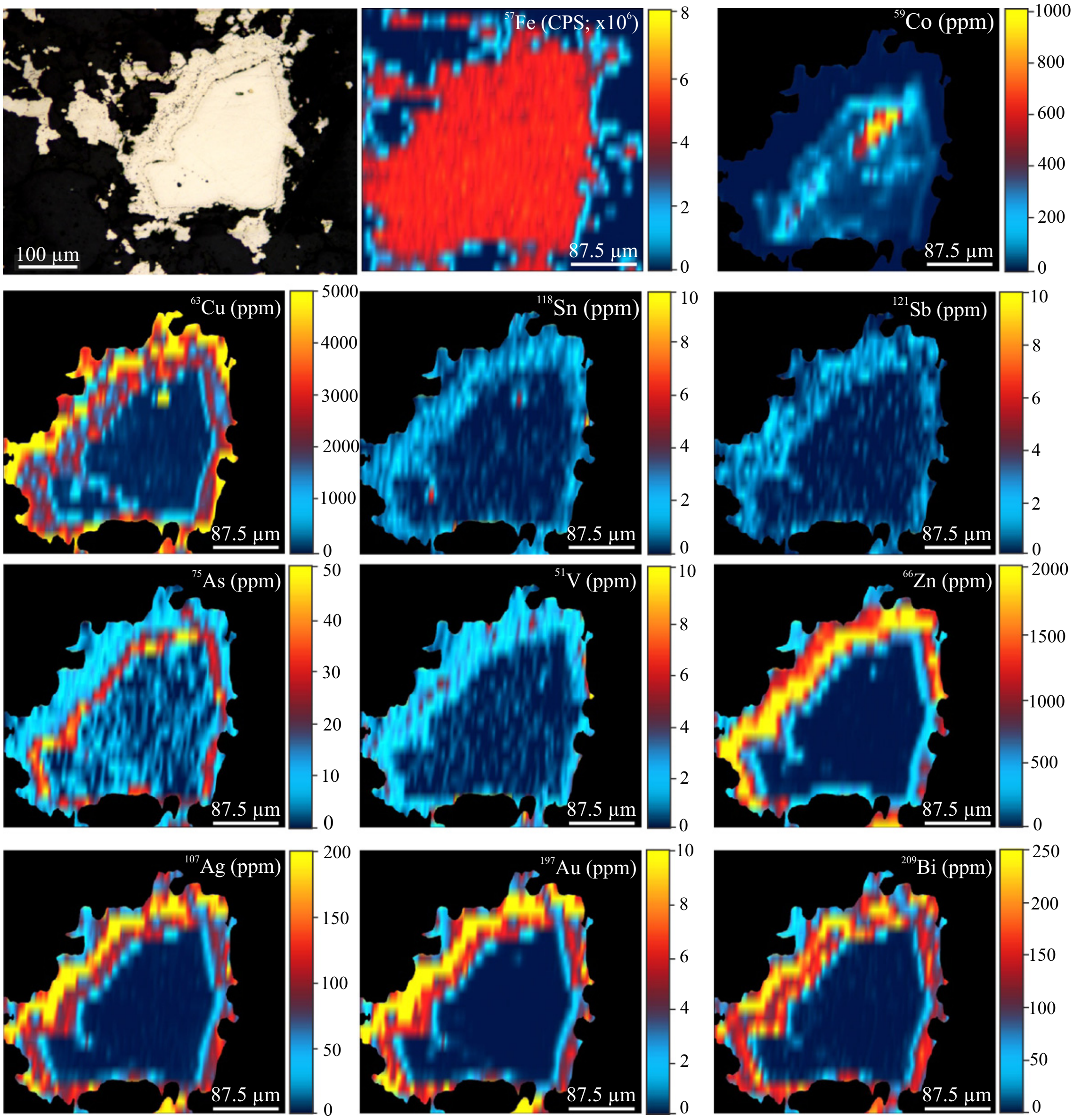

Fig. 11. LA–ICP-MS mapping of trace elements distribution (in ppm) in another zoned pyrite crystal from sample AR82-146 m (Fig. 2) with similar trace element enrichment and distribution. Note a V, Mo, Sn, and Sb enriched sector of the crystal's outer most rim. CPS: counts per second. The first picture shows a reflected light microphotograph of the analyzed pyrite crystal.

with some irregular boundaries and numerous vugs (dissolved micro-inclusions) in their cores, suggesting that they progressively underwent chemical overprinting by retrograde reaction or dissolution. This type of texture has been reported in pyrite from several epithermal deposits (e.g., Carrillo Rosúa et al., 2003; Freitag et al., 2004; Pačevski et al., 2012) and from a Cu–Au skarn overprinted by a younger hydrothermal event that produced oxidation, silicification, argillization, and sulfidation (Cepedal et al., 2008).

Pyrites from the jigsaw breccia (AR82-359 m) and the clast-supported hydrothermal breccia (AR82-265 m) are enriched in Cu (up to 2961 and 1076 ppm; respectively) compared to pyrite from the phyllic halo (up to 14 ppm Cu; sample AR9-187 m) (Table 1), and correlate with the highest grades of hypogene Cu (up to 3.7% Cu) in the section (Franchini et al., 2011; Fig. 2). The LA–ICPMS ablation profiles (Fig. 6) and the trace-element maps of one of these pyrites (AR82-265 m; Fig. 7) show distinctive zones enriched in Cu, V, Sn, As, Sb, or Pb, Zn, Ag, Au, and Bi that can be associated with sulfosalts inclusions. One such inclusion is colusite that contains V and Sn (2.95–3.13 wt.% V and 4.61–6.60 wt.% Sn). The compositional maps also show a zonation in trace metals defined by a Co-rich core, a mid-section enriched in Cu, and a rim enriched in Zn and minor Au (Fig. 7). The compositional and textural features described before are consistent with previous reports showing an intimate association between porosity in pyrite and the occurrence of inclusions of sulfosalts and multiple-metal inclusions, on both micro- and nano-scales (e.g., Deditius et al., 2011).

At shallower levels (AR82-160–96 m), pyrite in colloform bands and veinlets and marcasite precipitated during the latest stage of epithermal mineralization are unusually rich in trace metals that correlate with the highest Zn, Pb, Au, and Ag grades of the analyzed section (Fig. 2). These pyrites occur as either successive colloform bands on earlier, gold-free pyrite cores, or very fine-grained, irregularly shaped grains in the cement and in the late veinlets. Based on textural and mineral chemical data, the Co-bearing cores that are depleted in trace elements are interpreted as representing relict pyrite fragments from the early porphyry stages (potassic–phyllic). Most analyzed colloform pyrites from the breccias zone are As-poor (As contents are <30 ppm; Table 1). These pyrites are significantly depleted in As when compared to pyrites from the epithermal deposits, e.g., the low sulfidation epithermal

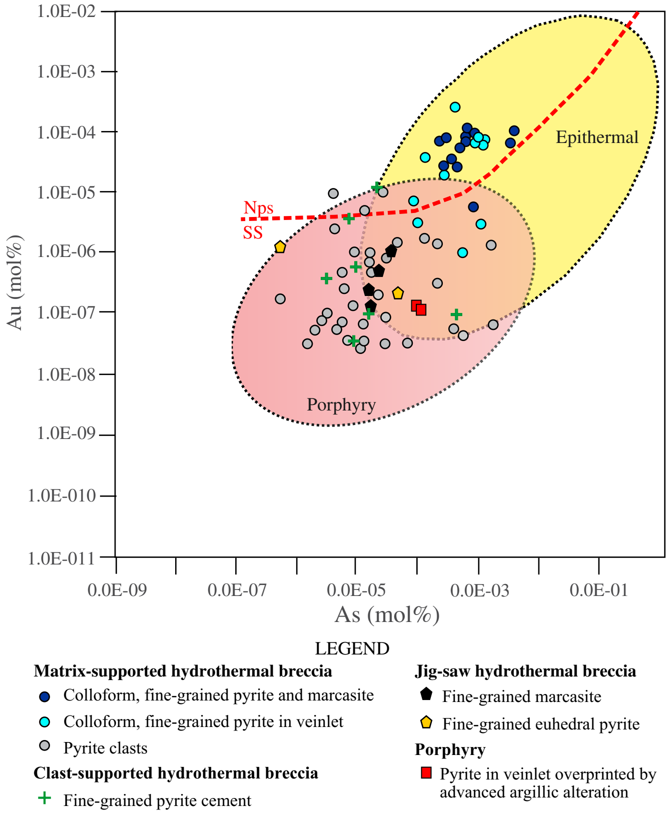

Fig. 12. Diagram showing Au–As relations in pyrite from the Agua Rica deposit. The red and yellow fields represent the range of Au–As concentrations of pyrites from porphyry and epithermal deposits worldwide, respectively (data taken from Deditius et al., 2014). The red segmented line is the solubility limit of Au as a function of As (Reich et al., 2005). While most pyrite samples plot below the solubility limit, late-stage colloform pyrites plot above this boundary. See text for details.

deposit of Emperor in Fiji (up to 16.60 wt.% As; Pals et al., 2003), and the high sulfidation deposits of Palai-Islica, Spain (up to 6.11 wt.% As; Carrillo Rosúa et al., 2003), El Dorado, Chile (up to 1.96 at.% As; Carrillo Rosúa et al., 2003), Yanacocha, Perú (up to 5.5 wt.%; Deditius et al., 2009), Pueblo Viejo, Dominican Republic (up to 3.04 wt.%; Deditius et al., 2011) and the Čoka Marin, Serbia (up to 4 wt.% As; Pačevski et al., 2012), or in quartz stockwork veins with high As content (up to 4.5 wt.% As; Zachariáš et al., 2004). The highest As values in this study were measured in a pyrite core from a clast (52.5 ppm in sample AR82-147 m; Table 1) and in late marcasite (up to 90.2 ppm in samples AR82-96 m; Table 1). All this evidence suggests relatively low activity of As in the hydrothermal fluids in this stage.

Another interesting fact related to the chemical zoning of these late pyrites (maps in Fig. 10) is that As concentration is preferentially distributed along a thin (inner) growth band within the thicker trace element-rich rim. Zinc is enriched following As depletion (Fig. 11). Previous studies have demonstrated that "invisible" gold in pyrite from a large variety of ore deposits is spatially associated with local enrichment in As (e.g., Deditius et al., 2014; Fleet et al., 1989, 1993; Mumin et al., 1994; Palenik et al., 2004; Reich et al., 2005; Simon et al., 1999). Among other likely mechanisms (e.g., semiconducting and/or redox surface effects), chemisorption may have played a role in efficiently removing Au and other trace metals from ore fluids onto As-rich bands in colloform pyrite, as suggested by Fleet and Mumin (1997).

One significant feature of these colloform bands is their high Pb (up to 4528 ppm) and Cu (up to 3900 ppm) contents. The LA–ICPMS profiles for Pb and Cu of Fig. 7 show some irregularities that appear to be related to inclusions of discrete Pb and Cu-bearing minerals. For example, elevated Pb contents in pyrite from the epithermal Palai-Islica, Yanacocha, Pueblo Viejo, and Côka Marin epithermal deposits were reported by Carrillo Rosúa et al. (2003) (up to 0.5 wt.%), Deditius et al. (2008) (up to 0.4 wt.%), Deditius et al. (2011) (up to 0.76 wt.%), and Pačevski et al. (2012) (up to 7 wt.%), respectively. Lead was found substituting isovalently for Fe in crystallites of As-bearing pyrite (Deditius et al., 2008) or as micro- to nanoscale inclusions – mainly Pb-(±As, Ag, Cu) sulfosalts – in pyrite that hosts lead and other trace elements (Deditius et al., 2011; Pačevski et al., 2012). At the Côka Marin deposit, Pačevski et al. (2008) found pyrites with band-like texture, oscillatory and rarely sector-zoning patterns that contain structurally bound copper (up to 8 wt.% Cu) substituting for Fe. Copper (up to 1.26 wt.%) also occurs in the late stages of pyrite crystallization (as collomorphic pyrite) in the Palai-Islica deposit associated with the deposition of non-stoichiometric As by colloidal precipitation (Carrillo Rosúa et al., 2003). Other examples of epithermal deposits where pyrite contains high Cu are Pueblo Viejo (up to 2.76 wt.% Cu; Deditius et al., 2011), Nukundamu (10 wt.% Cu), Cerro de Pasco (up to 1.5 wt.% Cu; see Pačevski et al., 2008 and references therein). In the ore-stage pyrite from the high-sulfidation Pascua deposit in Chile and part of Argentina, enrichment patterns of Cu (up to 0.42 wt.% Cu) are mainly antithetic to those of As (up to 0.60 wt.%; Chouinard et al., 2005). Based on SIMS depth-profiling and EMPA WDS mapping in Cu-rich pyrite, Reich et al. (2013) suggested that Cu concentrations in excess of ~10,000 ppm (~1 wt.%) were most likely related to the presence of sub-micrometer particles and nanoparticle aggregates of chalcopyrite or other Cu-bearing sulfide minerals.

Zinc reaches 1078 ppm in late pyrites from this breccia zone at Agua Rica (1045 ppm in colloform bands and 1078 ppm in stringer). Some LA–ICPMS signals for Zn of colloform pyrites are smooth (Fig. 9A, E, F) and others are ragged (Fig. 9B, C, D), indicating either its homogeneous distribution within solid solution or its presence as Zn-bearing inclusions. The porous and the collomorphic pyrites of the epithermal Palai-Islica deposit have relatively large amounts of Zn (up to 0.39 and 0.18 wt.%, respectively); Zn in the porous pyrite correlates with Au–Ag alloys and in the colloform variety correlates with Ag, Cu, Ni, and As concentrations (Carrillo Rosúa et al., 2003). As-rich pyrite from the early precious metal stage at El Dorado epithermal deposit contains up to 0.48 wt.% Zn (Carrillo-Rosúa et al., 2008). At the Yanacocha epithermal deposit, stage 3 pyrite contains as much as 3600 ppm Zn (Deditius et al., 2009).

"Invisible" Au and other metals in the colloform band sand fine-grained (veinlet, stringer) pyrites at Agua Rica are up to 6.7 ppm Au, 136 ppm Ag, 1077 ppm Bi, and 3.1 ppm Te. The ablation profiles of these bands indicate that at the scale of each spot, Au can be homogenously distributed (Fig. 9A, C, E, F) or as micro-scale inclusions (Fig. 9D) with Bi and Ag (Fig. 9D). This is consistent with predictions of Au speciation in pyrite using Au–As relations in Section 7.1 (Fig. 12). At Palai-Islica there is a low content of "invisible" Au in the pyrite (up to 160 ppm), but there is a relatively large amount of Ag in the pyrite (up to 1.47 wt.%) associated with marcasite and in the collomorphic pyrite (up to 0.20 wt.%; Carrillo Rosúa et al., 2003). At Pueblo Viejo, the As-rich growth zones of pyrite contain up to 1600 ppm Ag, 900 ppm Sb, 600 ppm Hg, 300 ppm Te, and 200 ppm Se, whereas precious metal (Ag with smaller amounts of Au) and Pb-rich nanoparticles with additional trace elements, including Pb–Sb–Bi–Ag–Te–S and Pb–Te–Sb–Au–Ag–Bi–S, were observed in Cu-rich and barren pyrite (Deditius et al., 2009). Similarly, atYanacocha Au (up to 0.10 at.%) in pyrite is concentrated in the As^{3+}-rich zones of colloformic overgrowths (Deditius et al., 2008). Pyrite from the Porgera epithermal deposit, in Papua New Guinea, hosts nanoparticles consisting of Pb–Ag–Sb–S, Sb–Pb–S, and PbS (Deditius et al., 2011). Ore-stage pyrite in the Pascua deposit contains up to 0.41 wt.% Ag and 386 ppm Au (Chouinard et al., 2005); gold has a stronger relation with Cu and Se, while As is associated mainly with Ag, and Te with Se. In the Emperor deposit the concentrations of Au (up to 11,057 ppm, with average of

507 ppm), and Te (up to 5796 ppm) in pyrite are extraordinarily high (Pals et al., 2003). The elevated Au content of pyrite may be due to the presence of As-rich marcasite or arsenopyrite lamellae in its structure or to Au being adsorbed in telluro–gold complexes (Pals et al., 2003).

7.3. Fluid composition and incorporation of trace elements in pyrite

At Agua Rica, the most elevated trace element concentrations in colloform pyrite occur in the hydrothermal breccia at shallow levels, along with late stage Bi–Pb–Cu sulfosalts, marcasite, sphalerite, and "invisible" Au and Ag. This matrix-supported breccia with rock flower and minor hydrothermal cement that hosts the analyzed pyrite and marcasite, is a product of a high degree of mixing and milling of fragments, which indicates the highest zone of energy released of the examined breccias. These processes may have been repeated several times during the protracted magmatic hydrothermal activity at Agua Rica as is indicated by breccia in breccia textures and the various generations of alunite and pyrite (Franchini et al., 2011). The Au–As signature of pyrite in hydrothermal ore deposits has been used by Reich et al. (2005) and more recent studies to constrain the saturation state of Au-bearing fluids from which arsenian pyrite precipitated. Within this context, the Au–As data in pyrite at Agua Rica shown in Fig. 12 supports a hydrothermal evolution where ore fluids forming early pyrite were undersaturated with respect to native Au (solid solution incorporation), while later fluids precipitating colloform pyrite where supersaturated with respect to native Au (Au nanoparticles).

Colloform texture – initially explained by colloidal deposition – has found to be formed under non-equilibrium, kinetically controlled conditions (Fleet et al., 1989), and represents changes in the ore fluid or in the precipitation conditions (Craig and Vaughan, 1994). Thus, the colloform banding in pyrite from this breccia zone may reflect rapid crystallization during fluid boiling and/or fluid mixing, creating large temperature fluctuations and producing undercooling in the mixed fluid. Hydrothermal fluids were supplied by continued fluid pathways generated by brecciation. These shallow fluids were already depleted in As and Cu (this breccia zone does not contain covellite or enargite cement, in contrast to the deeper zones of the jigsaw or clast supported-breccias; Fig. 2) and may still have had very high activity of sulfur, high fO_2, and /or pH < 5 to precipitate alunite (Stoffregen, 1987) and marcasite (Murowchick and Barnes, 1986). The low concentration of Fe in sphalerite (0–0.51 wt.% Fe; Franchini et al., 2011) in this breccia, also indicates high sulfidation state /or high oxygen fugacity of the late stage fluids (Czamanske, 1974; Einaudi et al., 2003). The conditions produced by dilution of the ore fluids by meteoric waters are conducive to H_2S and HS^- generation and consequently, marcasite precipitation (at temperatures less than 240 °C, pH less than 5), and sulfide species partially oxidized, or reacted with more-oxidized sulfur species (Murowchick and Barnes, 1986). The trace elements in pyrite and marcasite – Pb, Cu, Zn, Bi, and Ag – are part of the low temperature chalcophile group of bismuth sulfosalts and tellurides, minerals that can carry invisible Au (Ciobanu et al., 2009). Thus, the metal-bearing inclusions documented in this study in colloform pyrites may be viewed as the final sinks for trace elements remobilized during the waning stage of the epithermal mineralization in the Agua Rica deposit (Franchini et al., 2011).

Recent work on pyrites from the high sulfidation epithermal Pueblo Viejo and Yanacocha deposits (Deditius et al., 2009) found alternating and multiple As-rich (with Au, Ag, Sb, Te, and Pb), Cu-rich, and barren growth zones reflecting abrupt changes in fluid composition. These changes have been interpreted to be the result of mixing between the pyrite-forming fluid and vapor that invaded the main hydrothermal system episodically. The As-rich vapor formed at high and possibly magmatic temperatures, whereas the Cu-rich vapor formed at lower temperatures, possibly during migration of the original magmatic vapor (Deditius et al., 2009). More recently, well-developed oscillatory zoning has been detected in pyrite from the Dexing porphyry Cu (Mo–Au) deposit in China, where Cu-rich, As-depleted growth zones alternate with Cu-depleted, As-rich layers. Such features are consistent with geochemical decoupling of Cu and As–Au, suggesting that selective partitioning of metals into pyrite is the result of changes in hydrothermal fluid composition (Reich et al., 2013). Furthermore, mineralogical evidence from the Côka Marin polymetallic, high sulfidation epithermal deposit indicates that entrapment of nanoscale Pb-bearing inclusions in pyrites was attributed to abrupt changes in ore-forming conditions and rapid co-precipitation of metal sulfides in a sub-volcanic environment (Pačevski et al., 2012). At the Yanacocha deposit in Perú, the presence of Au-bearing As^{3+}-bearing pyrite suggests that the hydrothermal fluids were acidic, oxidized and undersaturated with respect to native gold (Deditius et al., 2008).

8. Conclusions

We have described the textures and trace-element distributions within pyrite and marcasite from the polymetallic Agua Rica deposit in time and space. Pyrite formed throughout the ore-deposit evolution from early porphyry to the latest stages of epithermal mineralization. Using SEM–BSE imaging coupled with LA–ICPMS analysis, the major- and trace-element composition of various pyrite crystals and marcasite were constrained and then compared to literature data for such minerals in typical epithermal deposits. Pyrites from all the epithermal sub-stages at Agua Rica are much lower in arsenic than most other epithermal deposits and this may reflect its preferential incorporation into enargite.

Early pyrites from the porphyry stage are fine-grained and trace element-poor. Pyrite crystals that precipitated during the high sulfidation mineralization stages are texturally complex and have significantly more elevated concentrations of trace elements. In the jigsaw and the clast-supported hydrothermal breccias with the highest grades of hypogene Cu, pyrite crystals are enriched in Cu and contain inclusions of sulfosalts and multiple-metal inclusions. In the hydrothermal breccias at shallow levels, late colloform bands and veinlets of pyrite and marcasite are rich in trace metals that correlate with the highest Zn, Pb, Au, and Ag grades of the analyzed section. These pyrite and marcasite precipitated in the highest zone of energy released of the examined breccias, probably during fluid boiling and mixing with meteoric waters. These shallow fluids had temperatures < 240 °C, high fS_2 and fO_2, pH < 5, and were depleted in As and Cu but supersaturated with respect to native Au (Au nanoparticles). Thus, the metal-bearing inclusions documented in colloform pyrites may be viewed as the final sinks for trace elements remobilized during the waning stage of the epithermal mineralization in the Agua Rica deposit.

We have demonstrated that the systematic correlation between texture and trace element variations in pyrite provides key information related to the chemical evolution of hydrothermal fluids from the porphyry to epithermal stages. When combined with detailed geological information and mineralogical observations, our data shows that the trace metal composition of pyrite can be used as a monitor of the ore environment and a proxy for fluid composition variations, which can be used both as a vector for exploration and as a tool for better understanding the genesis of giant hydrothermal ore deposits.

Acknowledgments

This work forms part of a project financed by Consejo Nacional de Investigaciones Científicas y Técnicas Argentino (PIP n° 6043 and PIP n° 1083) and Universidad Nacional del Comahue (n° 04/I167 and 04/I002). David Lentz and Chris McFarlane are supported by a Natural Sciences and Engineering Research Council Discovery Grant. We express our appreciation to Dr. Yan Luo (UNB) for helping with the acquisition of the LA–ICP-MS data, to Ross Large and Richard Goldfarb for their helpful and constructive reviews which led to further improvement of the manuscript.

Appendix A. Supplementary data

Supplementary data to this article can be found online at http://dx.doi.org/10.1016/j.oregeorev.2014.10.022.

References

Allmendinger, R.W., 1986. Tectonic development, southeastern border of the Puna Plateau. Geol. Soc. Am. Bull. 97, 1070–1082.

BHP, 1999. The Agua Rica porphyry Cu–Mo–Au deposit, Catamarca. Geology and Mineral Resource Update. Internal Report (420 pp.).

Bissig, T., Lee, J.K.W., Clark, A.H., Heather, K.B., 2001. The Cenozoic history of volcanism and hydrothermal alteration in the central Andean flat-slab region: new ^{40}Ar–^{39}Ar constraints from the El Indio-Pascua Au (Ag, Cu) belt, 29° 20′–30° 30′ S. Int. Geol. Rev. 43, 312–340.

Caelles, J.C., Clark, A.H., Farrar, E., McBride, S.L., Quirt, S., 1971. Potassium–argon ages of porphyry copper deposits and associated rocks in the Farallón Negro-Capillitas district, Catamarca, Argentina. Econ. Geol. 66, 96–964.

Carrillo Rosúa, F.J., Morales Ruano, S., FenollHach-Ali, P., 2003. Iron sulphides at the epithermal gold–copper deposit of Palai-Islica (Almera, SE Spain). Min. Mag. 67, 1059–1080.

Carrillo-Rosúa, J., Morales-Ruano, S., Morata, D., Boyce, A.J., Belmar, M., Fallick, A.E., FenollHach-Alí, P., 2008. Mineralogy and geochemistry of El Dorado epithermal gold deposit, El Sauce district, central-northern Chile. Miner. Petrol. 92, 34–360.

Cepedal, A., Fuertes-Fuente, M., Martin-Izard, A., Gonzalez Nistal, S., Barrero, M., 2008. Gold-bearing As-rich pyrite and arsenopyrite from the El Valle gold deposit, Asturias, northwestern Spain. Can. Mineral. 46, 233–247.

Chouinard, A., Williams-Jones, A.E., Leonardson, R.W., Hodgson, C.J., Silva, P., Téllez, C., Vega, J., Rojas, F., 2005. Geology and genesis of the multistage high-sulfidation epithermal Pascua Au–Ag–Cu deposit, Chile and Argentina. Econ. Geol. 100, 463–490.

Ciobanu, C.L., Cook, N.J., Pring, A., Brugger, J., Danushevsky, L., Shimizu, M., 2009. Invisible gold in bismuth chalcogenides. Geochim. Cosmochim. Acta 73, 1970–1999.

Cook, N.J., Chryssoulis, S.L., 1990. Concentrations of “invisible gold” in the common sulfides. Can. Miner. 28, 1–16.

Cook, N.J., Ciobanu, C.L., Mao, J., 2009. Textural controls on gold distribution in As-free pyrite from the Dongping, Huangtuliang and Hougou gold deposits, North China Craton (Hebei Province, China). Chem. Geol. 264, 101–121.

Craig, J.R., Vaughan, D.J., 1994. Ore Microscopy and Ore Petrography, 2nd edition. John Wiley and Sons Inc., (423 pp.).

Czamanske, G.K., 1974. The FeS content of sphalerite along the chalcopyrite–pyrite–bornite sulfur fugacity buffer. Econ. Geol. 69, 1328–1334.

Deditius, A.P., Utsunomiya, S., Renock, D., Ewing, R.C., Ramana, C.V., Becker, U., Kesler, S.E., 2008. A proposed new type of arsenian pyrite: composition, nanostructure and geological significance. Geochim. Cosmochim. Acta 72, 2919–2933.

Deditius, A.P., Utsunomiya, S., Ewing, R.C., Chryssoulis, S.L., Venter, D., Kesler, S.E., 2009. Decoupled geochemical behaviour of As and Cu in hydrothermal systems. Geology 37, 707–710.

Deditius, A.P., Utsunomiya, S., Reich, M., Kesler, S.E., Ewing, R.C., Hough, R., Walshe, J., 2011. Trace metal nanoparticles in pyrite. Ore Geol. Rev. 42, 32–46.

Deditius, A., Reich, M., Kesler, S.E., Utsunomiya, S., Chryssoulis, S., Walshe, J.L., Hough, R., Ewing, R.C., 2014. The coupled geochemistry of Au and As in pyrite from hydrothermal ore deposits. Geochim. Cosmochim. Acta 140, 644–670.

Einaudi, M.T., Hedenquist, J.W., Inan, E., 2003. Sulfidation state of hydrothermal fluids: the porphyry–epithermal transition and beyond. In: Simmons, S.F., Graham, I.J. (Eds.), Volcanic, Geothermal and Ore-Forming Fluids: Rulers and Witnesses of Processes within the Earth. Soc. of Econ. Geol. and Geochem. Soc., Special Publication 10, pp. 285–313.

Fleet, M., Mumin, H., 1997. Gold-bearing arsenian pyrite and marcasite and arsenopyrite from Carlin Trend gold deposits and laboratory synthesis. Am. Miner. 82, 182–193.

Fleet, M.E., MacLean, P.J., Barbier, J., 1989. Oscillatory-zoned As-bearing pyrite from strata-bound and stratiform gold deposits: an indicator of ore fluid evolution. In: Keays, R.R., Ramsay, W.R.H., Groves, D.I. (Eds.), The Geology of Gold: The Perspective in 1988. Econ. Geol. 6, pp. 356–362.

Fleet, M.E., Chryssoulis, S.L., Maclean, P.J., Davidson, R., Weisener, G., 1993. Arsenian pyrite from gold deposits: Au and As distribution investigated by SIMS and EP, and color staining and surface oxidation by XPS and LIMS. Can. Miner. 31, 1–17.

Franchini, M.B., Impiccini, A., Lentz, D., Ríos, F.J., O'Leary, S., Pons, J., Schalamuk, I.A., 2011. Porphyry to epithermal transition in the Agua Rica polymetallic deposit, Catamarca, Argentina: an integrated petrologic analysis of ore and alteration paragenesis. Ore Geol. Rev. 41, 49–74.

Franchini, M.B., Impiccini, A., Beaufort, D., Patrier, P., Anderson, C., Pons, J., 2012. Mineral assemblages and distribution of phyllosilicates composition along the main section of the Agua Rica deposit, Catamarca, Argentina. Implications for future mine developments. Appl. Clay Sci. 67–68, 61–71.

Freitag, K., Boyle, A.P., Nelson, E., Hitzman, M., Churchill, J., Lopez-Pedrosa, M., 2004. The use of electron backscatter diffraction and orientation contrast imaging as tools for sulfide textural studies: example from the Greens Creek deposit (Alaska). Miner. Deposita 39, 103–113.

Gregory, M.J., Lang, J.R., Gilbert, S., Hoal, K.O., 2013. Geometallurgy of the pebble porphyry copper–gold–molybdenum deposit, Alaska: implications for gold distribution and paragenesis. Econ. Geol. 108, 463–482.

Jordan, T.E., Allmendinger, R.W., 1986. The Sierra Pampeanas of Argentina: a modern analog of rocky mountain foreland deformation. Am. J. Sci. 286, 737–764.

Koukharsky, M., Mirré, J.C., 1976. Mi Vida prospect: a porphyry copper-type deposit in northwestern Argentina. Econ. Geol. 71, 849–863.

Landtwing, M., Dillenbeck, E., Leake, M., Heinrich, C., 2002. Evolution of the breccia-hosted porphyry-Cu–Mo–Au deposit at Agua Rica, Argentina: progressive unroofing of a magmatic–hydrothermal system. Econ. Geol. 97, 1273–1292.

Large, R.R., Danyushevsky, L., Hollit, C., Maslennikov, V.V., Meffre, S., Gilbert, S., Bull, S., Scott, R., Emsbo, P., Thomas, H., Singh, B., Foster, J., 2009. Gold and trace elements zonation in pyrite using Laser Imaging Technique: implications for the timing of gold in orogenic and Carlin-style sediment-hosted deposits. Econ. Geol. 104, 635–668.

Maydagán, L., Franchini, M.B., Lentz, D., Pons, J., McFarlane, C., 2013. Sulfide composition and isotopic signature of the Altar Cu–Au deposit, Argentina: constraints on the evolution of the porphyry–epithermal system. Can. Miner. 51, 813–840.

McFarlane, C., Luo, Y., 2012. U–Pb geochronology using 193 nm excimer LA–ICP-MS optimized for in situ accessory mineral dating in thin section. Geoscience Can. 39, 158–172.

Mumin, A.H., Fleet, M.E., Chryssoulis, S.L., 1994. Gold mineralization in As-rich mesothermal gold ores of the Bogosu–Prestea mining district of the Ashanti Gold Belt, Ghana: remobilization of “invisible” gold. Mineral. Deposita 29, 445–460.

Murowchick, J.B., Barnes, H.L., 1986. Marcasite precipitation from hydrothermal solutions. Geochim. Cosmochim. Acta 50, 2615–2629.

Navarro, H., 1986. Geología general y económica del pórfido de cobre-molibdeno “Mi Vida”, Andalgalá, Catamarca. Rev. Inst. Geol. Univ. Nac. Jujuy 6, 127–154.

Pačevski, A., Libowitzky, E., Živković, P., Dimitrijević, R., Cvetković, L.J., 2008. Copper-bearing pyrite from the Čoka Marin polymetallic deposit, Serbia: mineral inclusions or true solid-solution? Can. Mineral. 46, 249–261.

Pačevski, A., Moritz, R., Kouzmanov, K., Marquardt, K., Živković, P., Cvetković, L., 2012. Texture and composition of Pb-bearing pyrite from the Čoka Marin polymetallic deposit, Serbia controlled by nanoscale inclusions. Can. Mineral. 50, 1–20.

Palenik, C.S., Utsunomiya, S., Reich, M., Kesler, S.E., Ewing, R.C., 2004. “Invisible” gold revealed: direct imaging of gold nanoparticles in a Carlin-type deposit. Am. Miner. 89, 1359–1366.

Pals, D.W., Spry, P.G., Chryssoulis, S., 2003. Invisible gold and tellurium in arsenic-rich pyrite from the Emperor gold deposit, Fiji: implications for gold distribution and deposition. Econ. Geol. 98, 479–493.

Paton, C., Hellstrom, J., Paul, B., Woodhead, J., Hergt, J., 2011. Iolite: freeware for the visualisation and processing of mass spectrometric data. J. Anal. At. Spectrom. 26, 2508–2518.

Perelló, J., Rojas, N., Devaux, C., Fava, L., Etchart, E., Harman, P., 1998. Discovery of the Agua Rica porphyry Cu–Mo–Au deposit, Catamarca Province, northwestern Argentina, part II: geology. In: Porter, T.M. (Ed.), Porphyry and Hydrothermal Copper and Gold Deposits, A Global Perspective: Glenside, South Australia, Austral Mineral Foundation, Symposium, Perth, Western Australia, pp. 117–132.

Reich, M., Kesler, S.E., Utsunomiya, S., Palenik, C.S., Chryssoulis, S.L., Ewing, R.C., 2005. Solubility of gold in arsenian pyrite. Geochim. Cosmochim. Acta 69, 2781–2796.

Reich, M., Utsunomiya, S., Kesler, S.E., Wang, L.M., Ewing, R.C., Becker, U., 2006. Thermal behaviour of metal nanoparticles in geologic materials. Geology 34, 1033–1036.

Reich, M., Deditius, A., Chryssoulis, S., Li, J.W., Ma, C.Q., Parada, M.A., Barra, F., Mittermayr, F., 2013. Pyrite as a record of hydrothermal fluid evolution in a porphyry copper system: a SIMS/EMPA trace element study. Geochim. Cosmochim. Acta 104, 42–62.

Rojas, N., Perelló, J., Harman, P., Cabello, J., Devaux, C., Fava, L., Etchart, E., 1998. Discovery of the Agua Rica porphyry Cu–Mo–Au deposit, Catamarca Province, northwestern Argentina, part I: exploration and discovery. In: Porter, T.M. (Ed.), Porphyry and Hydrothermal Copper and Gold Deposits, A Global Perspective: Glenside, South Australia, Australian Mineral Foundation, Symposium, Perth, Western Australia, pp. 111–117.

Rosco, R., Koukharsky, M., 1999. El pórfiro cupro-molibdenífero Agua Rica y las manifestaciones epitermales asociadas, Catamarca. In: Zappettini, E. (Ed.), Recursos Minerales de la República Argentina: Instituto de Geología y Recursos Minerales, Buenos Aires, Anales 35, pp. 1479–1492.

Sasso, A.M., 1997. Geological Evolution and Metallogenetic Relationships of the Farallón Negro Volcanic Complex, NW Argentina(PhD thesis) Queen's University, Kingston, Ontario (843 pp.).

Sasso, A.M., Clark, A.H., 1998. Magmatic, hydrothermal and tectonic evolution and implications for Cu–Au metallogeny in the Andean back-arc. Soc. Econ. Geol. Newslett. 34 (1), 8–17.

Simon, G., Huang, H., Penner-Hahn, J.E., Kesler, S.E., Kao, L.S., 1999. Oxidation state of gold and arsenic in gold-bearing arsenian pyrite. Am. Miner. 84, 1071–1079.

Stoffregen, R.E., 1987. Genesis of acid-sulfate alteration and Au–Cu–Ag mineralization at Summitville, Colorado. Econ. Geol. 82, 1575–1591.

Urreiztieta, M., Rosello, E.A., Gapais, D., LeGorve, C., Cobbold, P.R., 1993. Neogene dextral transpression at the southern edge of the Altiplano–Puna (NW Argentina). II International Symposium on Andean Tectonics, Oxford. Editions de l'Office de la Recherche Scientifique et Technique d'Outre-mer, Paris, pp. 267–269.

Whitney, D.L., Evans, B.W., 2010. Abbreviations for names of rock-forming minerals. Am. Miner. 95, 185–187.

Zachariáš, J., Frýda, J., Paterová, B., Mihaljevič, M., 2004. Arsenopyrite and As-bearing pyrite from the Roudný deposit, Bohemian Massif. Min. Mag. 68, 31–46.

Zwahlen, C., Cioldi, S., Wagner, T., Rey, R., Heinrich, C., 2014. The porphyry Cu–(Mo–Au) deposit at Altar (Argentina): tracing gold distribution by vein mapping and LA–ICP-MS mineral analysis. Econ. Geol. 109, 1341–1358.